Journal of Energy Storage 92 (2024) 112222

Contents lists available at ScienceDirect

Journal of Energy Storage

journal homepage: www.elsevier.com/locate/est

Research Papers

Influence of thermal energy storage basins on the subsurface and shallow groundwater

Christoph Bott [a,*], Abdulrahman Dahash [b], Maximilian Noethen [a], Peter Bayer [a]

[a] Department of Applied Geology, Institute of Geosciences and Geography, Martin Luther University Halle-Wittenberg, Von-Seckendorff-Platz 3, 06120 Halle, Germany
[b] Center for Energy, AIT Austrian Institute of Technology GmbH, Giefinggasse 4, 1210 Vienna, Austria

ARTICLE INFO

Keywords:
Design optimization
Environmental impacts
Modeling and co-simulation
Seasonal thermal energy storage
Subsurface and groundwater
Water-gravel storage

ABSTRACT

Seasonal thermal energy storage for heat and cold supply is of growing importance in modern energy systems. Yet, high thermal losses and inadequate storage efficiencies hinder their market maturity. Especially under challenging conditions, e.g., due to groundwater flow, the accuracy of planning predictions is affected. Moreover, for subsurface installations, interaction with the subsoil cannot be sufficiently modeled, while operational risks can result when legal environmental thresholds are violated. Addressing these shortcomings, this study presents a new modeling and simulation framework to improve the design and operation of ground-based, sensible, seasonal thermal energy storage systems. Coupling two customized models via a co-simulation approach, both the internal storage (i.e., storage medium/structure) behavior as well as processes in the surrounding environment are resolved in detail. In this way, previously unconsidered mechanisms are unraveled allowing in-depth analyses regarding environmental impacts and interactions under various conditions. The study firstly introduces the newly developed tool, then secondly benchmarks its applicability in a subsequent parameter study, examining impacts under different hydrogeological conditions. Results show a broad efficiency range of 13 %, despite thermal insulation. In the case of uninsulated storage, efficiency is reduced by up to 24 %. Introducing a novel spatial differentiated analysis, influences of the groundwater saturated zone are quantified and temperatures of >45 °C in the 5 m distance of the storage are observed after 10 years of operation, whereby increased groundwater flow velocities are favorable to reduce impact intensities but also increase the affected area and the thermal losses. Along with the results of the case study, the presented framework provides a valuable tool for planning recommendations for future installations while offering a comprehensive assessment of various perspectives that have not been covered so far.

1. Introduction

Large-scale, seasonal thermal energy storage (sTES) is a key technology for realizing the transformation of the heating and cooling sector [1–3]. It is employed to combine different sources and sinks in an energy system, which are time shifts over days up to several months [4]. While seasonally solar charging is most common, other sources of energy cover continuous heat provision, e.g., by data centers, and geothermal installations, or variable and unpredictable loads, e.g., from industrial applications (Fig. 1c). Modern, 4th generation sTES also utilize intermittent charging/discharging processes in a dynamic range of temperatures and volumetric flow rates [5,6]. They are employed on different temporal and spatial scales together with district heating and cooling systems (DHC), ranging from small housing communities [7,8] to large districts with complex management of thermal energy provision [1,9–11].

The technological variants covered by this study are closed-loop, sensible systems. These utilize artificial reservoirs that can be further classified into Tank- (TTES), Pit- (PTES), and Water-Gravel Thermal Energy Storage (WGTES) [12–15]. All these types have mostly rectangular or cylindrical shapes and are designed as sloped basins, with a small surface area-to-volume (A_S/V) ratio, to minimize ambient heat loss. Typical volumes of TTES and WGTES are 5000 m^3 to 15,000 m^3, while PTES can comprise up to >200,000 m^3 [5,16]. The storages are commonly partially or completely buried underground, which is generally advantageous regarding thermal losses since thermal processes in the subsurface proceed more slowly than in the air and it often exhibits a higher average temperature over the year [17]. As a storage medium, TTES and PTES employ water only, while WGTES are filled

* Corresponding author.
E-mail address: Christoph.Bott@geo.uni-halle.de (C. Bott).

https://doi.org/10.1016/j.est.2024.112222
Received 30 October 2023; Received in revised form 25 April 2024; Accepted 20 May 2024
Available online 27 May 2024

Abbreviations and symbols

2D	Two dimensional
2.5D	2.5 dimensional
3D	Three dimensional
A	Area (m^2)
β	Groundwater inflow angle (°)
BC	Boundary condition
BGL	Below ground level (m)
c_p	Specific heat capacity (J kg^{-1} K^{-1})
δ_{ITC}	Inversed thermocline coefficient (W m^3 kg^{-1})
d	Diameter (m)
DHC	District heating and cooling
ε_p	Effective porosity
FMU	Functional mockup unit
G_m	Mass source (kg m^{-3} s^{-1})
g	Gravitational acceleration (9.81 m s^{-2})
H	Hydraulic head (m)
h	Height (m)
h^*	Relative height (%)
i	Hydraulic gradient (‰)
κ	Permeability (m^2)
k_{disp}	Dispersive thermal conductivity tensor (W m^{-1} K^{-1})
K	Hydraulic conductivity (m s^{-1})
λ	Thermal conductivity (W m^{-1} K^{-1})
l	Distance (m)
$l_{env,x/y}$	Characteristic side length in x and y direction (m)
L	(Characteristic) length (m)
μ	Dynamic viscosity (Pa s)
M	Layer thickness (m)
MUMPS	Multifrontal massively parallel sparse direct solver
η	Efficiency (%)
n	Normal vector on the boundary
P	Precipitation rate (mm h^{-1})
p	Pressure (Pa)
PE-X	Cross-lined polyethylene
Pr	Prandtl number
PVC	Polyvinyl chloride
PTES	Pit thermal energy storage
q_{ITC}	Inversed thermocline coefficient heat transport (W m^{-3})
$\ddot{q}$	Heat flow rate (W m^{-2})
$\dot{q}$	Heat flux (W m^{-1})
Q	Energy (Wh, MWh)
ρ	Density (kg m^{-3})
Re	Reynold's number
sTES	Seasonal thermal energy storage
θ	Volume fraction
σ_b	Stefan-Boltzmann constant (5.67 10^{-8} W m^{-2} K^{-4})
t	Time (h)
T	Absolute temperature (K)
TTES	Tank thermal energy storage
u	Darcy velocity (m s^{-1})
V	Volume (m^3)
$\dot{V}$	Volumetric flow rate (m^3 h^{-1})
v	Velocity (m s^{-1})
WGTES	Water-gravel thermal energy storage
ω	Surface emissivity
z	Elevation (m)

with a two-component mixture of gravel, sand or soil, and water. Thus, WGTES have a reduced storage capacity by about 20 % [18–20], but this is contrasted by the advantage that a self-supporting structure is created.

To prevent leakage and heat loss, all different variants are enclosed at all sides by a sealing liner (made of e.g., polyvinyl chloride (PVC), or stainless steel [21,22], depending on the temperature during operation), and by thermal insulation, which can be added with different thicknesses at the top, sidewall, and bottom. For WGTES, thermal insulation is usually the most cost-intensive part of a storage structure [22,23]. To allow an adequate integration of the installation into the landscape and to minimize heat loss, most of the TTES and WGTES have an external top cover, while the insulation is located inside [24–26]. Especially for steeply sloped geometries, additional static components are required. They are usually made of (possibly reinforced, prestressed) concrete and comprise a foundation, walls, and a roof. For operation, WGTES require indirect charging/discharging devices consisting of multiple levels of coil racks. In contrast, water-fillings are directly charged and discharged by extracting/re-injecting the storage medium through engineered stratification devices, that are less expensive [1,27–29]. Currently, the worldwide number of sTES is only just above 30 (with a total available storage volume of more than ca. 800,000 m^3), and they can be found mainly in Europe [5]. Progress toward technology improvements includes, for example, material and method optimization, as well as optimized integration into the DHC system, with combined short-term and long-term storage cycles and connection to multiple sources and sinks [1,11,30–32]. At the same time, however, these make the optimal basin structure and thus the planning and operation more complex, which underlines the need for efficient modeling tools [33–35].

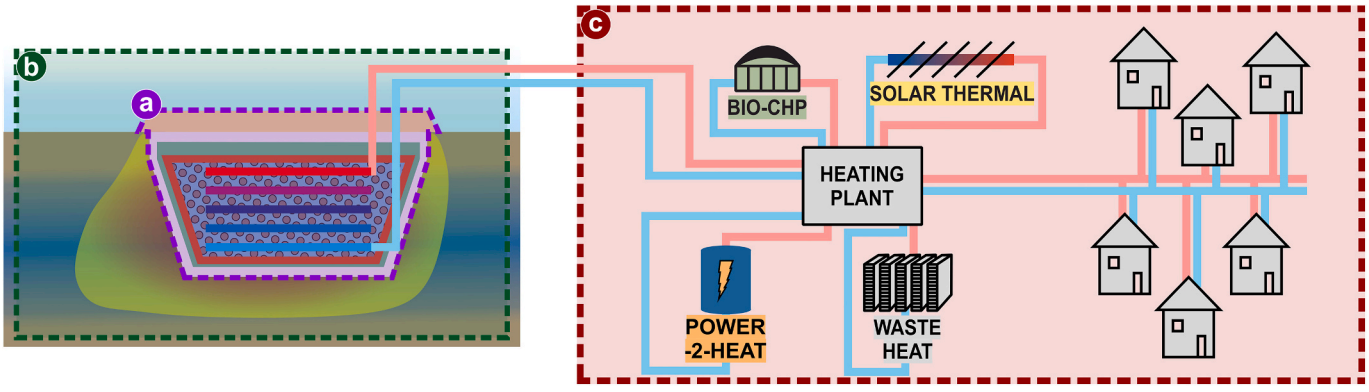

Fig. 1. Key modeling domains of sTES: a) seasonal thermal energy storage, b) surrounding environment, and c) energy system. BIO-CHP: combined heat and power plant based on bioenergy.

This study aims to tackle multiple key challenges in the planning process of sTES (Fig. 2). Addressing the technical perspective, past projects revealed that energy losses are often higher than expected and predicted by models (e.g., projects in Germany: Steinfurt-Borghorst [20], Friedrichshafen [20,36,37], Hamburg [37,38], Stuttgart [39]; Fig. 2a). Thus, a major challenge for simulation is the thermal interaction between the artificial storage basin, with the ambient natural subsurface and groundwater domain. Thermal conditions in both domains show at least seasonal patterns but differ greatly in variabilities and magnitudes. Planning is hindered by the challenge of coupling these domains in efficient models for reliable site-specific design optimization [40]. This underlines the need for more accurate simulation frameworks [41,42].

Environmental effects of sTES cover implications that evolve in the long term and may cause ecological concerns, such as increased mobility of contaminants [46,47], shifts in faunal community composition [48,49], and altered microbial abundances in groundwater [50] and drinking water distribution networks [51]. Despite their insulation, sTES embedded in the underground lead to increased temperatures in ambient soil (Fig. 2b) and, if present, groundwater bodies [52–54]. Especially for high-temperature applications subsurface temperatures of nearly 30 °C were observed (e.g., in Hamburg, Germany [20,44], Fig. 2b, and Friedrichshafen, Germany [20]). As a consequence, warming by sTES may affect groundwater quality and thus surpass legal threshold values ([52,55], Fig. 2c): various acceptable levels of heating are being discussed in research and refer to maximum temperatures (usually 20 to 25 °C) or temperature increases (3 K to 12 K) compared to the original state. Hence, standardized assessments are not available, and legal situations in European countries are diverse, as described by, e.g., [45,56,57]. This must be considered during the planning process, to comply with regulatory frameworks and approval permits.

The aim of this contribution is the development of a novel simulation framework, which depicts the operational behavior of sTES and their thermal interaction with the environment. The framework comprises an enhanced model for WGTES to be used to simulate interactions with groundwater flow. Hydrogeological and thermal transport processes are implemented in a tailored software configuration. With this, a more reliable planning and storage design is facilitated, while sensitivities of specific site conditions can be inspected. In the following, first, the developed model with its underlying concept and structure is introduced. Then, to demonstrate benefits of planning and operation, a parameter study to contrast technical and environmental characteristics under different hydrogeological settings is conducted.

2. Materials and methods

2.1. Modeling approach

The determination of the optimal sTES layout is a challenging and often evolving process, due to interconnected variables, which are often subject to change. For instance, Dahash et al. [1] revealed the interplay of location, size, geometry, and hydrogeological conditions for TTES and PTES. In this context, the choice of volume and geometry influences thermal losses, due to the A_S/V ratio, and the quality of thermal stratification, linked to the height-to-diameter (h/d) ratio. As sTES are often placed in the subsurface, this raises additional planning considerations, particularly regarding hydrogeological conditions (e.g., soil thermal conductivity, hydraulic conductivity, porosity, permeability, and groundwater flow angle). As a result, calibrated numerical sTES models play a necessary role in conducting such investigations. In this respect, Dahash et al. [58] compared sTES geometries, and found that a buried tank outperforms other geometries. Subsequently, their work was extended to consider groundwater flow, emphasizing the twofold impact of sTES-groundwater interaction, and the need for measures to prevent elevation in groundwater temperatures beyond legal thresholds [53]. However, these works demanded significant computational efforts. Sifnaios et al. [26] developed a simplified sTES model with a focus on short-term operations, using a temperature boundary condition (BC), based on monitoring data. This, however, neglects dynamic thermo-hydraulic interactions within the sTES' components. Consequently, that work did not address sTES simulation, potentially leading to misleading outcomes. As a consequence, no development so far covered a comprehensive simulation framework that dynamically integrates all sTES components with detailed subsurface conditions and groundwater flow.

The new framework is based on a co-simulation approach, where two complementary tools are combined [58]. First, the previously introduced “STORE” model [60] is employed for the sTES domain. Implemented in MATLAB/Simulink's Simscape library [59,60], it depicts a WGTES in 2.5 dimensions (2.5D) (i.e., vertical layers, and pre-defined, horizontal directions). Second, a three-dimensional (3D) numerical multi-physics model for simulating subsurface heat transfer and groundwater flow is implemented in COMSOL [61]. Third, the co-simulation is realized using a functional mockup unit (FMU) [62,63]. Advantages of the co-simulation result from flexible parameterization, which is integrated into the design database generation of STORE [64]. Optimal computational performance is achieved by allowing the models to operate at different time steps, depending on the complexity of both the sTES and the subsurface. The applicability of the new approach was assessed in a validation procedure (Appendix A). Thereby it was compared to a traditional methodology in which the storage facility is represented by temperature BCs in a numerical, 3D multiphysics model.

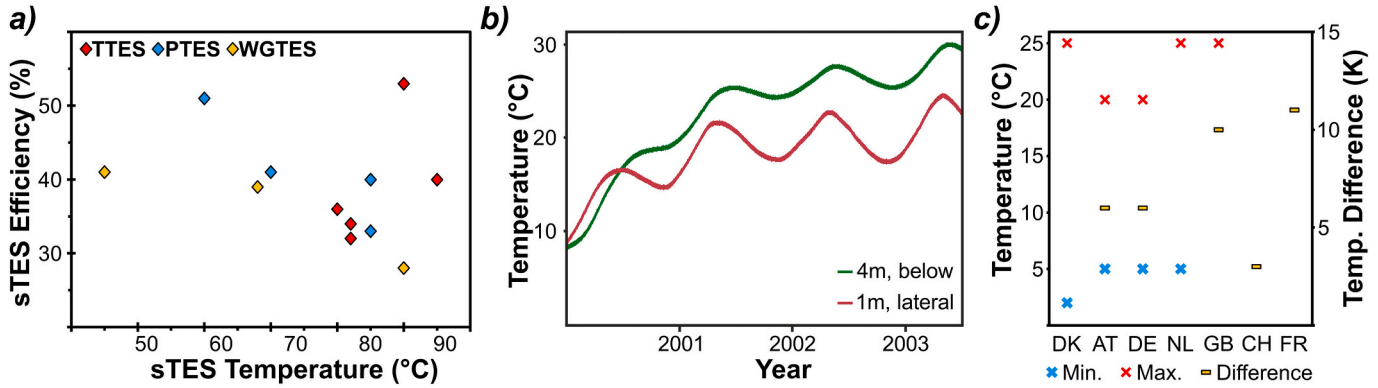

Fig. 2. Key issues reported for sTES basins: a) heat losses of different sTES installations (after [43]), b) observed ground temperatures in Hamburg, Germany (after [20,44]), and c) temperature regulations/recommendations for shallow geothermal energy applications in different countries as of 2010 (after [45]).

Besides minor discrepancies (−0.95 K to 3.12 K, mean deviation: 0.30 K) that are related to conceptual differences between the models (e.g. improved consideration of interactions and differing BC types of the new approach), a good agreement was demonstrated.

2.2. STORE model

Building on the first version of STORE [64], further developments are implemented to make the sTES simulation more accurate and flexible. The updated structure of the model is illustrated in Fig. 3. While the filling is represented in a vertically layered structure, it features a component-based resolution of all other components and relevant internal thermal processes. Nevertheless, weaknesses concerning model BCs and the setup are present: STORE is structured in four, pre-defined spatial directions (e.g., north, east, south, west) and does not consider hydrogeological BCs.

For the new framework, the number of storage layers was increased from 15 to 25. This is particularly relevant for facilities with a higher h/d ratio (i.e., a larger height) since the key feature of thermal stratification is stressed [36,65]. The temporal resolution is retained at one hour per step, allowing highly dynamic conditions of complex systems to be considered. Additionally, the representation of the processes within the filling is refined. During operation, layers with higher temperatures below layers with lower temperatures can occur. In this case, mixing is induced by free convection. This density-dependent inversed thermocline phenomenon is now implemented according to Eq. (1) (δ_{ITC}: inversed thermocline coefficient $= 10^5$ W m^3 kg^{-1}, ρ_{upper}, ρ_{lower}: density of the fluid in the upper/lower storage layer, V: volume of the layer) based on [66,67] (available, e.g., in the CARNOT Toolbox for MATLAB [68]).

$$\dot{q}_{ITC} = \delta_{ITC} \cdot (\rho_{upper} - \rho_{lower}) \cdot V \quad (1)$$

Concerning the included building components, a roof is added to the top layer of the model Additionally, to simulate operation utilizing an indirect coil heat exchanger, a new approach with two flow directions is employed. This considers that the flow direction between charging and discharging is commonly reversed to exploit thermal stratification, with high fluid temperatures being injected in and extracted from the top. Detailed pipe hydraulics are not considered.

For co-simulation, STORE is used exclusively for modeling the sTES structure. For all internal components, the necessary thermo-hydraulic processes through the sTES' shell are mapped. In contrast, this means that the top cover and the surrounding soil blocks as originally presented in [64] are now replaced by the COMSOL model. The default configuration of the model features a total of 448 nodes. Charging and discharging processes are represented directly via transient load profiles of temperature T and volumetric flow rates $\dot{V}$ or a controller, featuring an operation strategy with hysteresis settings. For the simulation, the design of the basin (including materials, dimensions, and material properties) and the load profiles are defined based on the specific site. In this context, in the application case, precise values based on actual characterizations are needed to ensure high-quality results. As an initial condition, it is assumed that the structure has a homogeneous temperature directly after construction and before commissioning, and that is in thermal equilibrium with the surrounding soil and groundwater temperature.

2.3. COMSOL model

Since the COMSOL model is used to represent the sTES environment, only the top cover is included as a sTES component. Still, this cover is important to avoid heat loss at the top [20,64,69]. By default, it features a 1 m overlap over the top surface of the sTES shell and a slope of 1:2 to the outside, to create a natural embankment. Other buildings on the ground surface are not included in the model, nor is the exact topography, which is approximated to a plane terrain.

The underground (Fig. 4) is divided into an unsaturated (vadose) zone, which is above the water table, and a saturated (phreatic) zone with groundwater flow governed by transient hydraulic heads. The lateral inflow and outflow sides of the model are defined at the opposite boundaries of the subsurface block, while the angle of inflow β is implemented by rotating the storage structure. Beyond this exemplary setup, it is possible to include different, site-specific conditions, e.g., by changing the geometry or the definition of other BCs. Conversely, further complexities of the subsurface (e.g., layers with less or higher permeability) and of groundwater flow (e.g., flow angle, table depth) can be flexibly included.

Consequently, the hydraulic gradient i results from the hydraulic heads at the model boundaries $H_{upgradient}$, $H_{downgradient}$ and the boundary distance l:

$$i = \frac{H_{upgradient} - H_{downgradient}}{l} \quad (2)$$

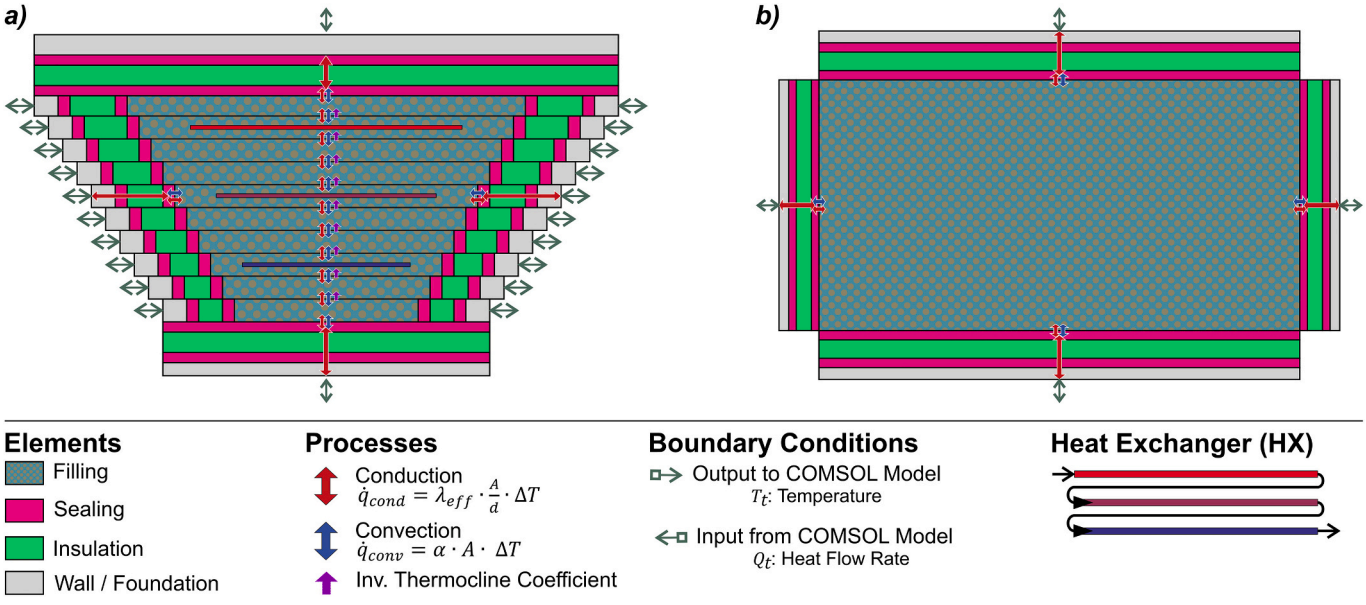

Fig. 3. Sketch of the STORE model for simulating WGTES, modified for the co-simulation framework in cross-sectional view (a) and top view on one layer (b).

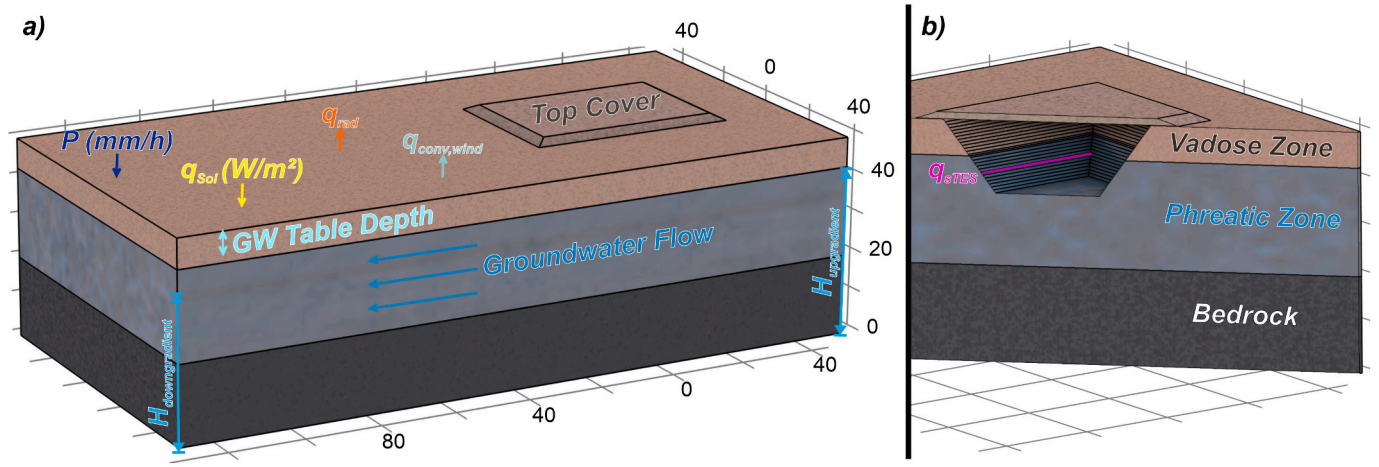

Fig. 4. a) Side, and b) cut plane view of the COMSOL model with top cover, unsaturated (vadose) zone, groundwater domain (phreatic zone), and bedrock layer, tailored for co-simulation. GW: groundwater, H: hydraulic head, P: precipitation, q: heat flux boundary condition.

At the bottom, a bedrock or aquitard is assumed, which delineates the aquifer. The model extensions are three to four times the basin dimensions in width and length, and three times the sTES height h_{sTES}. Further, the sTES is positioned at an asymmetrical distance to the boundaries so that the evolving thermal plume can evolve properly (Fig. 4).

For model setup and representation of the groundwater flow and thermal transfer processes in the subsurface, all geometry (layer thickness M) and material properties of the surrounding soil are required. These include density ρ, effective thermal conductivity λ_{eff}, specific heat capacity c_p, surface emissivity ω, hydraulic conductivity K, permeability κ, and porosity ε_p. To represent the groundwater regime, the angle of inflow, and initial environmental conditions (air and ground temperature) are required. This requires sufficiently accurate hydrogeological and meteorological measurement data when the framework is applied to specific case studies. Despite this, it is important to note that more complex (hydro-)geological conditions may imply sensitivity analyses about the uncertainties involved to ensure real-world applicability of the results.

Based on this parameterization, fundamentally important processes that most existing sTES simulation tools do not depict are modeled. These include Darcy's groundwater flow (mass transport through porous domains) with pressure p as the dependent variable. The mass source term G_m is calculated based on the fluid's density ρ, its dynamic viscosity μ, and the matrix's permeability κ and porosity ε_p:

$$G_m = \frac{\partial}{\partial t}(\rho \cdot \varepsilon_p) + \nabla \cdot (\rho \cdot u) \text{ with Darcy velocity } u = -\frac{\kappa}{\mu}\nabla p \tag{3}$$

Dirichlet conditions are set at the inflow and outflow boundaries to generate the hydraulic head distribution based on Eqs. (2) and (4). To calculate a pressure p, the known hydraulic head at the boundary H_0 is specified as a function of the elevation z, the gravitational acceleration g (9.81 m s^{-2}) and the groundwater density ρ:

$$p = \rho \cdot g \cdot (H_0 - z) \tag{4}$$

The other model boundaries are specified as no-flow boundaries, which define a zero Darcy's velocity u of the fluid according to its density ρ at a no-flow boundary with normal vector n:

$$-n \cdot \rho \cdot u = 0 \tag{5}$$

However, this does not apply to the soil surface, where a precipitation rate P with the same density as the groundwater is set as an inflow BC:

$$\rho \cdot P = -n \cdot \rho \cdot u \tag{6}$$

Thermal transfer processes in the porous subsurface are divided into a fluid and a matrix fraction assuming local thermal equilibrium. Thereby, the dependent variable of temperature T is used to model the processes of conduction, dispersion, and advection. Based on the above-described calculation of the coupled Darcy's velocity field u, the effective specific heat capacity $(\rho \cdot c_p)_{eff}$ (Eq. (7), ε_p: porosity, ρ_f: groundwater density, $c_{p,f}$: groundwater specific heat capacity, θ_s: volume fraction of the matrix, ρ_s: matrix density, $c_{p,s}$: specific heat capacity of the matrix, θ_{imf}: volume fraction of immobile groundwater in porous media, ρ_{imf}: density of the immobile fluid in porous media, $c_{p,imf}$: specific heat capacity of the immobile fluid in porous media, the heat flow rate q, Eq. (8)), with effective (volume-average) thermal conductivity λ_{eff} (Eq. (9), λ_s: thermal conductivity of the matrix, λ_{imf}: thermal conductivity of the immobile fluid in porous media, k_{disp}: dispersive thermal conductivity tensor (assumed isotropic) σ_b: Stefan-Boltzmann constant), the governing equation for the energy balance is shown in Eq. (10).

$$(\rho \cdot c_p)_{eff} = \varepsilon_p \cdot \rho_f \cdot c_{p,f} + \theta_s \cdot \rho_s \cdot c_{p,s} + \theta_{imf} \cdot \rho_{imf} \cdot c_{p,imf} \tag{7}$$

$$q = -\lambda_{eff} \cdot \nabla T \tag{8}$$

$$\lambda_{eff} = \varepsilon_p \cdot \lambda_f + \theta_s \cdot \lambda_s + \theta_{imf} \cdot \lambda_{imf} \text{ with } \lambda_s = \frac{\lambda_b}{\theta_s} \tag{9}$$

$$Q = (\rho \cdot c_p)_{eff} \cdot \frac{\partial T}{\partial t} + \rho_f \cdot c_{p,f} \cdot u \cdot \nabla T + \nabla \cdot q \tag{10}$$

STORE's original environmental processes (solar irradiation as heat flux boundary $\ddot{q} = -n \cdot \ddot{q}_{sol}(t)$, n: normal vector on the boundary), and radiation from the storage surface as surface-to-ambient radiation based on Eq. (11) with ω: surface emissivity, σ_b: Stefan-Boltzmann constant, as well as the interaction with the air (as temperature BC $T = T_{air}(t)$ are transferred to this model.

$$-n \cdot q = \omega \cdot \sigma_b \cdot \left(T_{air}^4(t) - T_{ground}{}^4\right) \tag{11}$$

Further, these BCs are expanded to include forced and natural convection by wind (Eq. (12), v_{wind}: wind speed, μ_{air}: dynamic viscosity, Pr: Prandtl number, Re: Reynold's number), based on a convective heat flux boundary, whereby an averaged heat transfer coefficient is calculated based on the assumption of external forced convection at a plate with a characteristic length L (Eq. (13), $l_{env,x}$, $l_{env,y}$: side length in x and y direction).

$$\ddot{q} = h \cdot (T_{air}(t) - T) \text{ with } h$$

$$= \begin{cases} 2 \cdot \frac{\lambda_{air} \cdot 0.3387 \cdot Pr^{1/3} \cdot Re_L^{1/2}}{L \cdot \left(1 + \left(\frac{0.0468}{Pr}\right)^{2/3}\right)^{1/4}} & \text{if } Re_L \leq 5 \cdot 10^5 \\ 2 \cdot \frac{k}{L} \cdot Pr^{1/3} \left(0.037 \cdot Re_L^{4/5} - 871\right) & \text{if } Re_L > 5 \cdot 10^5 \end{cases} \quad \text{with } Pr$$

$$= \frac{\mu_{air} \cdot c_{p,air}}{\lambda_{air}} \text{ and } Re_L = \frac{\rho_{air} \cdot v_{wind} \cdot L}{\mu_{air}} \tag{12}$$

$$L = \frac{l_{env,x} \cdot l_{env,y}}{2 \cdot l_{env,x} + 2 \cdot l_{env,y}} \tag{13}$$

For application cases, particularly in the case of non-uniform terrain (changed radiation angle and convection behavior) or buildings on the ground (no solar radiation, but insulation of the ground surface), these BCs may need to be adjusted. Transient weather data at an hourly resolution is required for specifying the BCs, including air temperature T_{air}, wind speed v_{wind}, solar irradiance $\ddot{q}_{sol}$, and precipitation P. This data is converted by the co-simulation to mean values according to the step size of the COMSOL model. Similarly, to properly represent groundwater flow, the hydraulic heads are based on a transient dataset of groundwater levels at the inflow and outflow boundaries, based on precise groundwater monitoring to ensure sufficient accuracy of the simulation results.

Since flow and transport processes in soil are slower than inside the storage [26,53], a temporal resolution of multiple days can be used. Besides, spatial mesh refinement in the near field of the storage is needed. The top cover consists of at least four layers, and, by default, 25 boundary layers per direction are advised around the sTES. Further mesh refinement strategies are presented in Appendix B, although potential sensitivities of different meshing might need to be checked when applying the tool.

2.4. Implementation

For efficient coupling, the chosen interface is the outer shell of the sTES. Accordingly, the following input and output data of the models are exchanged during simulation: In STORE, the heat flux $\dot{q}_{sTES}$ is recorded in each layer and in each predefined spatial direction, as well as above the roof and below the foundation, and transferred to the COMSOL model. In COMSOL, this heat flux is used as BC (i.e., thermal load) at contact surfaces (Fig. 4b), which depict the layered surfaces around the sTES. A reflection from COMSOL is obtained as a temperature probe (integrated average of the relevant temperature T_{ground}) at these surfaces, and these values are used as BCs in STORE for the next calculation step. Thus, the complexity of the interactions between the storage facility and the subsurface can be better resolved compared to traditional models, as required especially for asymmetric groundwater flow (i.e., inflow/outflow, vadose, and phreatic zones). Preliminary testing showed that a communication step size of min. 48–120 h can be considered adequate to prevent numerical fluctuations and generate accurate simulation results. For instance, 48 h is calculated in STORE, followed by simulation of a 48-h time frame in COMSOL. STORE operates with a variable step size solver (ode23t, max. step size 1 h). In COMSOL, a relative tolerance of 0.01 and an absolute tolerance of 0.005 are used. For every individual simulation per communication timestep, an initial step of one hour and a maximum step size of 20 h are specified. The direct solver MUMPS (multifrontal massively parallel sparse direct solver) is used to achieve a fast simulation.

After simulation, the results are evaluated with both tools, but it is advantageous to include the results of specific COMSOL probes in the STORE results database to enable joint evaluations. The evaluation in COMSOL focuses on the evolving thermal and hydrogeological conditions in 3D. Thus, point temperature probes are considered first, which are placed 2 m and 5 m adjacent to the storage wall at a height of ($0.5 \cdot h_{sTES}$). Heat losses $\ddot{q}$ are used as further indicators and are separated into sidewalls (phreatic and vadose sections), and top and bottom surfaces. In a two-dimensional (2D) perspective, a sectional plane is placed in horizontal orientation at a height of ($0.5 \cdot h_{sTES}$). There, thermoclines at 20 °C and + 6 K compared to ambient soil temperatures are used to check for violations of legal threshold values [45,70]. In STORE, the evaluation is in line with the procedure described by [64] and includes operation states, the filling temperature, as well as the storage efficiency $\eta_{storage}$, defined as the ratio of discharged vs. charged energy quantities.

For the simulation of a seasonal storage operation, a minimum time frame of at least five to ten years is suggested [35,41], since during a heat-up period the surrounding subsurface is warmed. This period is necessarily longer for uninsulated sTES with intensive interaction with the ambient ground. After that, a quasi-stationary state is expected, in which the heat losses, averaged over longer periods, are nearly constant [41,44,64].

2.5. Parameter study: impact of groundwater flow on seasonal thermal energy storage

2.5.1. Storage design

Starting from a baseline scenario, the following parameter study includes various assumptions for environmental conditions, to investigate general impacts of groundwater flow parameters. The full design scenario databases with all scenario definitions are provided in Appendix C, while material properties of all sTES components are summarized in Table 1 and based on standard literature values. As the materials selected are already utilized at existing facilities, their parameters provide a representative selection; moreover, some of them were already used in a previous study on the STORE model [54] and therefore offer comparability of results.

The considered WGTES system is located in Ingolstadt, Germany, where the re-use of an existing basin structure is planned. This strategy has previously been discussed to reduce construction, renovation, and/or demolition costs [71–73]. The basin is completely buried in the subsurface, whereas the roof's top surface conforms to ground level. For ideal landscape integration, it features an external top cover of soil (same material as unsaturated zone, cf. Table 1), with 1.5 m thickness and a slope angle of 1:2, overlapping the rim by 1 m. The storage facility is located in an area with no buildings and on flat terrain. After its conversion, it is assumed to be in thermal equilibrium with its environment. The geometry of the basin represents an inverted truncated pyramid with a slope angle of 1:0.5. The side lengths are arranged in a ratio of 3:2:1 (length/width/height = 45 m/30 m/15 m), resulting in a filling volume of 11,814 m^3.

As filling, a water-saturated matrix of gravel is considered. The

Table 1
Material properties of the example storage facility. Values used for filling material according to the WGTES installation in Chemnitz, Germany [19,20], and for foam glass gravel according to a manufacturer's data sheet ([74], ideal conditions assumed).

Component	Material	Density ρ (kg m^{-3})	Effective thermal conductivity λ (W m^{-1} K^{-1})	Specific heat capacity c_p (J kg^{-1} K^{-1})
Filling	Water saturated gravel	1928	2.40	1545
Insulation	Foam glass gravel	160	0.05	900
Sealing	PVC	1900	0.48	900
Static components	Concrete	2600	1.00	1000
Heat exchanger	PE-X	930	0.41	1900

material properties used are in line with the investigated construction material of the reported site in Chemnitz [19,20] and the previous study by Bott et al. [64]. To account for natural convection induced by density differences, an effective heat transfer coefficient $\delta_{ITC} = 20$ W m^{-2} K^{-1} is assumed. To prevent thermal energy loss, apart from the external top cover, the sTES is equipped with an internal, all-sided insulation consisting of the commonly used material foam glass gravel [5,6,74]. As the thermal stratification is expected to result in the highest temperatures in the upper part, a top thickness of 0.5 m is employed, while the bottom insulation is 0.1 m thick. Also, the insulation of the sidewalls is decreased from 0.3 m to 0.1 m from top to bottom. The sidewalls and bottom insulation are excluded in an uninsulated scenario. The thermal insulation material is embedded inside compartments of a sealing material, to protect it from moisture penetration [75]. This has been implemented, for example, in Steinfurt-Borghorst, Germany [20] and Hannover, Germany [76]. The supposed re-use of a basin structure implies an additional structural component. Made of cast reinforced concrete, both the walls and the roof measure 0.2 m in thickness, while the foundation is assumed to be 0.3 m thick. An indirect coil heat exchanger on five levels at relative heights of $h^*_{sTES} = 12$ %, 32 %, 52 %, 72 %, and 92 % with a diameter of 0.05 m and internal distances and a distance to the external wall of each 0.5 m, is included. Its total length amounts to 8729 m and the resulting surface area A_S is approximately 2742 m^2. The pipe material is cross-lined polyethylene (PE-X), and the thickness of the pipe wall measures 0.0025 m.

2.5.2. Storage operation

The sTES is operated referring to a real dataset of energy demands of different commercial, as well as industrial processes. Thereby, the volumetric flow rates and inlet temperatures of the charging/discharging load profiles are scaled to the storage volume, assuming that only a partial load of the DHC is used for optimum integration. The resulting charging and discharging datasets are presented in Fig. 5.

The storage is not operated on a strictly seasonal cycle but highly dynamic, comprising intermediate charging and discharging phases for buffering peak loads. With 5053 h in one year of operation, more charging hours are given than for discharging (1707 h), while in 2000 h, the sTES is in standby mode. Further, charging is dominating in the summer months and, with approx. 0.08 to 36.15 m^3 h^{-1} (mean 12.65 m^3 h^{-1}) and temperatures between 62.5 and 90.0 °C (mean 84.14 °C), more intensive than the discharging profile. The latter is operated between temperatures of 36.1 to 52.3 °C (mean 43.3 °C) and volume flow rates of 0.0056 m^3 h^{-1} to 23.38 m^3 h^{-1}. Time or temperature hysteresis is not considered.

2.5.3. Ambient environmental conditions

The site represents an unconfined sedimentary aquifer. The required material properties for the different domains are presented in Table 2. A 20 m thick bedrock layer is assumed to be a solid rock (e.g., granite). Above, the saturated zone with flowing groundwater consists of sandy gravel. The topmost part (vadose zone) consists of the same material as the saturated zone. Assuming a groundwater table depth of 50 % of the sTES height, the aquifer thickness is 7.5 m. For the emissivity of thermal energy by radiation, it is assumed that the ground is sparsely vegetated, represented by a surface emissivity coefficient of $\omega = 0.95$ [77].

Datasets for specifying environmental BCs are gained from publicly available databases of the German Weather Service (Fig. 6).

Table 2
Material properties of the surrounding subsurface around the storage facility.

Domain	Density ρ (kg m^{-3})	Effective thermal conductivity λ (W m^{-1} K^{-1})	Specific heat capacity c_p (J kg^{-1} K^{-1})	Effective porosity ε_p	Hydraulic conductivity K (m s^{-1})
Bedrock	2600	2.9	850	10^{-10}	10^{-10}
Phreatic zone	2600	3.758	795.4	0.43	10^{-4}
Vadose zone	1500	2.2	800	0.43	10^{-4}

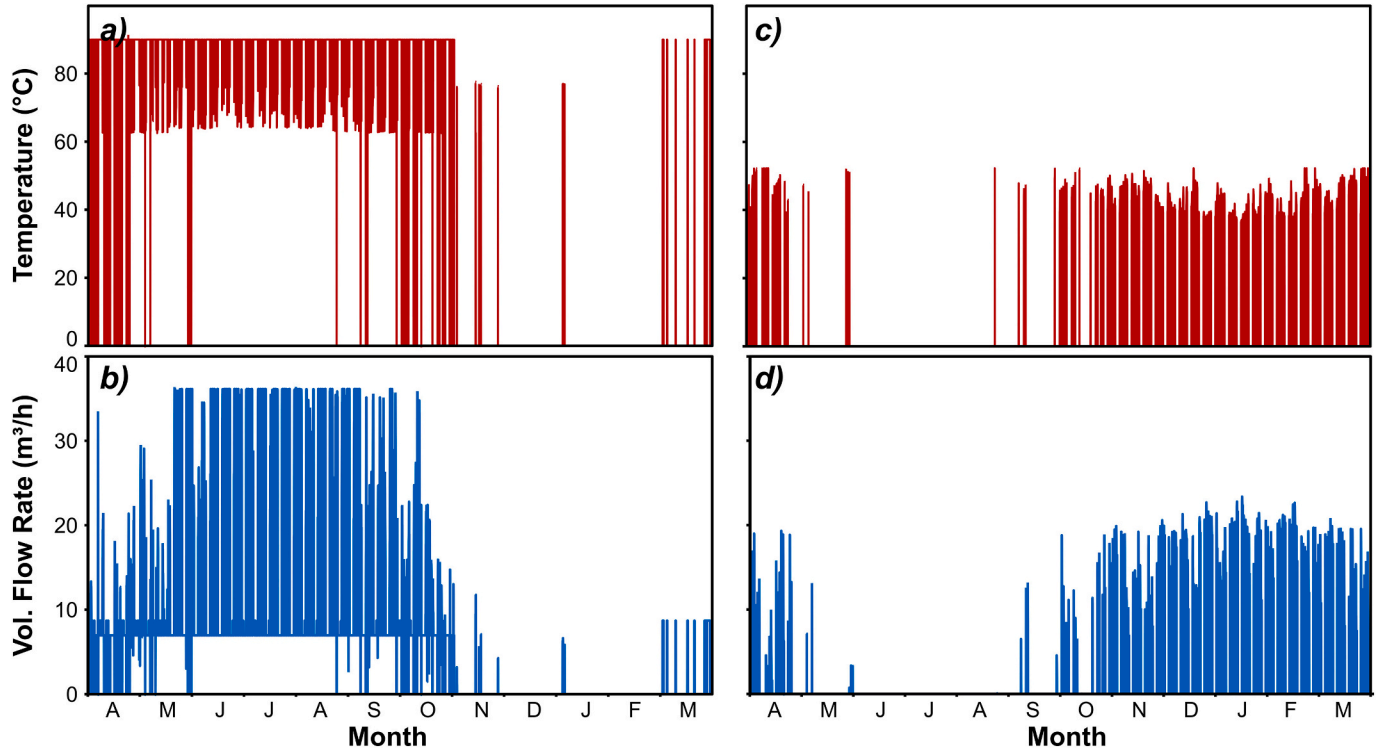

Fig. 5. Operation data for the parameter study, consisting of available temperatures (a and b, in °C) and volumetric flow rates (c and d, in m^3 h^{-1}) for charging (a and c) and discharging (b and d).

Meteorological data of the test reference years [78,79] contain wind speed, air temperature, and diffuse solar irradiance. For precipitation and ground temperature data, long-term hourly mean values of a nearby weather station are incorporated. Seasonality is apparent in temperature and solar radiation datasets, justifying the design of a sTES at the considered location.

2.5.4. Scenario definitions

The scenarios presented in Table 3 list variable hydrogeological conditions that may affect the sTES. In the base case, the insulated sTES are approached by groundwater from the short side of the basin (i.e., 0°), with a mean groundwater table depth of 50 % of the height of the basin (i.e., 7.5 m below ground level (BGL)). The groundwater flow is moderate with a hydraulic gradient of 2 ‰ (= 0.2 %). In further scenarios, the parameters varied relate to the groundwater flow direction ($\beta = 90°$, i.e., inflow approaching the basin's wide side), the groundwater level (20 % vs. 50 % of h_{sTES}), and the hydraulic gradient (0 ‰, i.e., stagnant water, and 5 ‰). One scenario (V5) is used to investigate a constant, high groundwater flow velocity of 10^{-5} m s^{-1}. In contrast, scenario NoGW inspects when groundwater flow is ignored or cannot be modeled. To emphasize the effects of basin insulation, an uninsulated scenario (top insulation only, I0) is included as an extreme case. For all insulated scenarios, the time communication step size is set to 5 days, while the uninsulated scenario is simulated with a communication step size of 2 days, due to much steeper temperature contrasts between the sTES and the subsurface. The simulated period is set to 10 years for all scenarios.

3. Results and discussion

3.1. Base case

In the base case (overview of model results in Fig. 7), the sTES shows a storage efficiency of $\eta_{storage} = 42.5$ % over the entire simulation period of 10 years. During all charging phases, a total of 5289 MWh is injected into the storage, whereas the discharged energy amounts up to 2248 MWh (Fig. 8). The heating phase can be observed by an increase of the subsurface temperatures (Fig. 7), and, likewise, the storage efficiency shows an improvement, from 24.4 % in the first year up to 46.9 % in the last year of the investigated operation period. Over the entire study period, the average temperature of the filling is 63.1 °C.

Visually, a stable temperature stratification in the sTES storage medium can be observed. The maximum temperature reached in the last year is 81.1 °C. In contrast, the minimum temperature in the last year is 39.5 °C, resulting in a total capacity of 411 MWh (Fig. 8). The specific energy losses that occur in the 10th year are highest at the bottom (108.2 kWh m^{-2}). In comparison, they are 80.9 kWh m^{-2} at the sidewalls and 57.8 kWh m^{-2} at the top, proving the significant influence of insulation thicknesses. As a result, effective insulations are of utmost importance, especially at the top of sTES, to mitigate thermal interference surroundings. Also, a more accurate spatial allocation can be made: In the phreatic zone, heat losses are on average 92.9 kWh m^{-2}, which is 17.9 % higher than in the vadose zone (76.3 kWh m^{-2}). As discussed by previous studies (e.g., [54]) this is linked to the higher thermal conductivity due to water saturation, and enhanced by significant impacts of groundwater flow (e.g., Darcy flow velocity and advection).

Due to the lateral basin insulation, the sTES walls (Fig. 7) show a slower temperature increase (ca. 0.8 K a^{-1}), further highlighting the conceptual necessity of this component for technical improvements. At the same time, the duration of the heating phase for ambiance is considerably longer (Fig. 9). For temperatures at a depth of 7.5 m BGL ($0.5 \cdot h_{sTES}$) and 2 m distance (Fig. 9, top), this can be observed well: Although an exceedance of a 20 °C threshold is observed after 14.6 months at 2 m distance, this occurs only after 19.7 months at a distance of 4 m. Similar values of ca. 21.6 °C in a distance of 1 m after 13.9 months were also observed for the more insulated sTES in Hamburg [20,44], while the simulation study by Sifnaios et al. [26] indicated temperatures of 20 °C at a depth of 8 m at ca. 7 m distance after 11 to 23 months. However, their model uses a less realistic temperature BC at the sTES walls and does not simulate the sTES itself, thus neglecting ambient-sTES interactions. Further, the scenario of their study covered an uninsulated PTES, leading to direct temperature progression into the

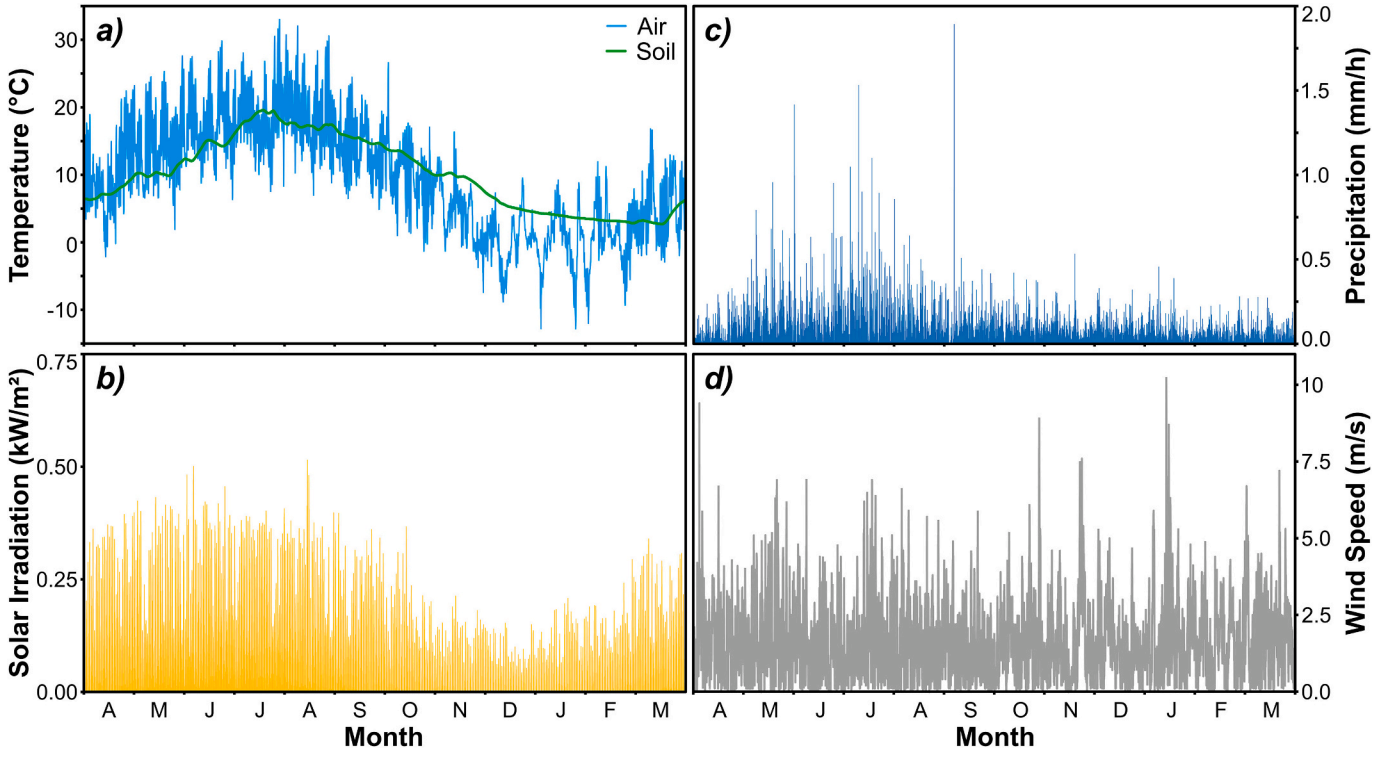

Fig. 6. Environmental data used in the case study, consisting of a) temperatures for soil and air, b) solar irradiation, c) precipitation, and d) wind speed.

Table 3
Scenarios for parameter study with variations of different groundwater (angle of inflow/0° short side, 90° wide side, groundwater table depth, groundwater flow gradient) and insulation scenarios. (BGL: below ground level, h_{sTES}: sTES height).

ID	Groundwater inflow angle β (°)	Groundwater table depth (% h_{sTES})	Groundwater flow gradient (‰)	Storage insulation
1: Base	0	50 (=7.5 m BGL)	2	Yes
2: G00	0	50	0	Yes
3: G50	0	50	5	Yes
4: V5	0	50	$u = 10^{-5}$	Yes
5: A90	90	50	2	Yes
6: H20	0	20 (=12 m BGL)	2	Yes
7: I0	0	50	2	No
8: NoGW	n.a.	n.a.	n.a.	Yes

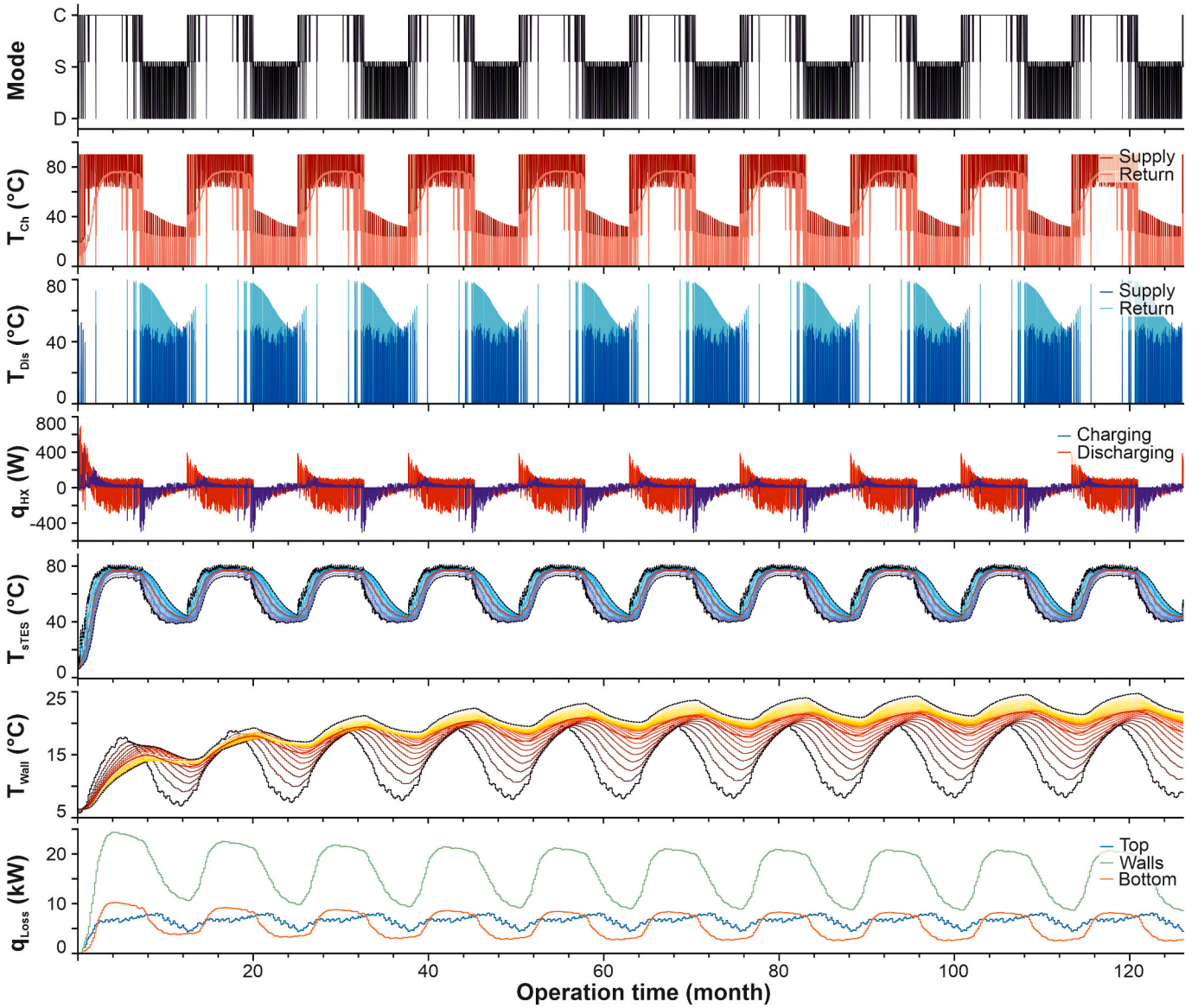

Fig. 7. Result of the sTES operation for the base case scenario over 10 years. From top to bottom: mode of operation (C: charging, S: standby, D: discharging), charging and discharging temperature, heat exchanger (HX) heat flow, sTES filling and wall temperatures (both layer-resolved, red dotted line: mean temperature, black dashed lines: maximum and minimum temperatures), thermal losses. (For interpretation of the references to color in this figure legend, the reader is referred to the web version of this article.)

ambient soil.

3.2. Technical perspective

Effects of different hydrogeological parameters become evident in performance characteristics. In Fig. 8, values of the energy balance of the sTES, storage efficiency levels, temperature ranges, and peak capacity levels during the last simulated year are presented. The results reveal that groundwater flow has a significant impact on sTES facilities. Despite moderate insulation in both scenarios, compared with the base

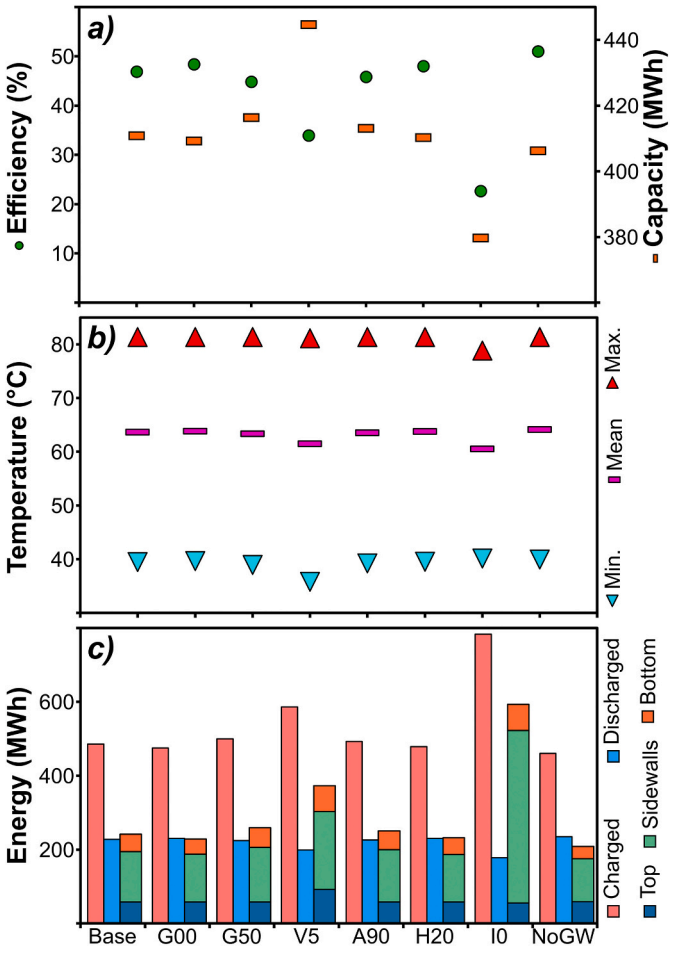

Fig. 8. Key performance indicators for comparison of the different scenarios (cf. Table 3) of the parameter study: a) efficiency and simulated maximum capacity, b) filling temperatures (min., mean, max.), c) values of the sTES energy balance (charged, discharged, and lost energy quantities at the top, sidewalls, and bottom).

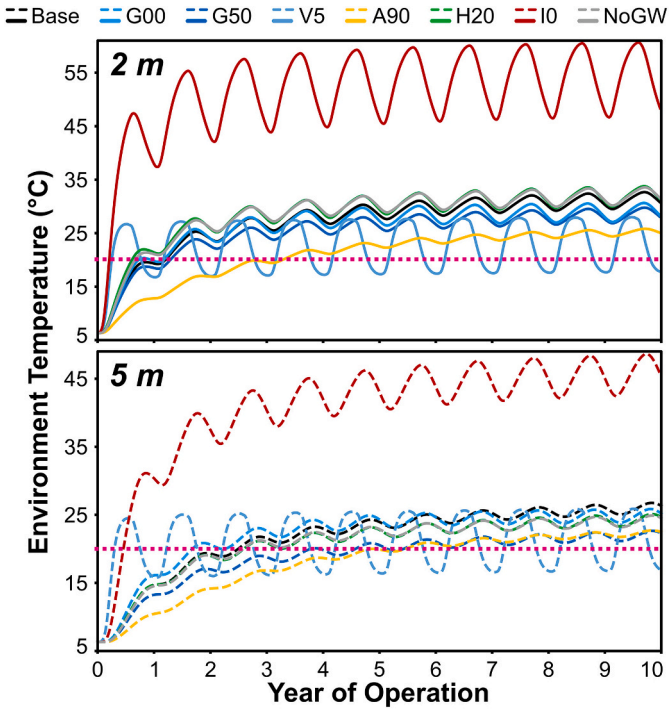

Fig. 9. Impacts of sTES on subsurface: environment temperatures in 2 m (solid lines), and 5 m (dashed lines) distance. The pink dotted lines indicate the legal threshold value of 20 °C for Germany and Austria. (For interpretation of the references to color in this figure legend, the reader is referred to the web version of this article.)

case, the NoGW scenario has a 4.1 % higher storage efficiency (51.0 %). While Dahash et al. [80] reported an efficiency decrease of about 15 % for uninsulated PTES, this value is in accordance with a more efficiently insulated TTES in a subsequent study by Dahash et al. [53]. However, both studies focus on different sTES technology types. For the NoGW case, 7.0 MWh more energy can be discharged, and the mean filling temperature increases up to 64.2 °C. Over the total simulation time frame, the increase in discharged energy equals 62 MWh (2310 MWh vs. 2248 MWh in the base case), which is 15.3 % of the sTES' capacity. Moreover, inspection of the energy losses shows that due to the heat transport by groundwater (i.e., advection), the sidewalls' contribution to thermal losses increases by ca. 20 MWh (116.9 MWh vs. 136.6 MWh in the base case) and bottom (32.7 MWh vs. 46.8 MWh in the base case), while they are almost constant at the storage's top (58.4 MWh vs. 57.8 MWh in the base case).

In general, the results compiled in Fig. 8 show that the individual hydrogeological parameters do not lead to high disparities. Indeed, varying sensitivities of the factors exist, however, for moderate changes of the conditions, no extensive effects are evident. For this study, this is due to the thermal insulation, minimizing energy loss and impacts on the environment. A stagnant groundwater body (scenario G00) leads to a decrease in storage efficiency of 2.6 % in the 10th year compared to the scenario without presence of groundwater. While such values were not reported for long-term operations of WGTES before, this is in line with recent findings of Sifnaios et al. [26], where it was found that stagnant groundwater leads to increased thermal losses of around 14 % for an uninsulated PTES, while groundwater flow can raise thermal losses to around 60 %.

Apart from the uninsulated case (see below), the ranges of resulting storage efficiency values for scenarios with groundwater influence in the last simulated year extend from 34.0 % (V5) to 48.0 % (G00). Therein, for the latter scenario, 68.3 MWh of lost energy is in contrast to a charged energy amount of 475.6 MWh. In the worst case, these values amount to 111.5 MWh and 585.9 MWh, respectively. This also has an impact on the filling mean temperatures, ranging from 61.0 °C to 63.2 °C over the total time frame. In contrast, in the 10th year, the largest temperature spread, and capacity of 444.6 MWh is achieved in scenario G00, which is 8.2 % more than for the base case.

Nevertheless, the groundwater flow velocity is identified as the most influencing factor. Compared with the base case, the storage efficiency is reduced by 12.9 % in scenario V5. Again, this is related to the phreatic zone, where specific heat losses are increased by 55.5 % to 144.4 kWh m^{-2}. In general, for increased flow velocities, due to a shorter residence time of the groundwater, the thermal plume propagation is extended, however, the temperature gradient between the ambient soil and the sTES wall is increased. Adverse effects in the last simulated year, as the decrease of discharged energy of 12.6 % (198.9 MWh vs. 227.6 MWh in the base case), further prove a lower amount of available energy. This general trend is apparent as well for variable hydraulic gradients, which govern the groundwater flow velocity. There, peak capacity levels of the sTES are increased by about 3.57 %, when comparing a steeper gradient of 5 ‰ with a stagnant groundwater body. Similarly, higher energy losses in the 10th year are observed, especially for the sidewalls (G00: 129.0 MWh vs. G50: 148.0 MWh) and the bottom interface (G00: 41.3 MWh vs. G50: 53.7 MWh). In this case, the base case scenario lies in between, as a result of the intermediate hydraulic gradient of 2 ‰, and it can be concluded that high groundwater flow velocity leads to higher heat losses, but at the same time to lower ground temperatures.

Conversely, the smallest impact is observed for the groundwater

inflow angle, where the reduction in storage efficiency is only 1.0 % in the last simulated year, at higher losses of 250.1 MWh.

In contrast to this stands the effect of sTES insulation: Comparing the base case with the extreme case of an uninsulated sTES, the 10th-year storage efficiency is drastically decreased to only 22.7 % (24.2 % less than the base case). In this case, the average filling mean temperature is only 59.4 °C over 10 years of operation. In the 10th year, the maximum filling temperature is only 78.8 °C, while specific losses at the walls and at the bottom amount to 276.7 kWh m^{-2} and 163.5 kWh m^{-2}, respectively. Consequently, in the case of groundwater impacts, sidewall and bottom insulation are indispensable for WGTES, and for other sTES types. Besides, other design recommendations to mitigate impacts of groundwater flow on sTES may represent cut-off walls (e.g., for PTES, as in line with findings by Dahash et al. [53]), to achieve reasonable efficiency.

3.3. Environmental perspective

Effects of different hydrogeological parameters also become evident in the impact analysis of the sTES on its surrounding soil. The different angles of inflow and hydraulic gradients lead to different groundwater velocity distributions. Thus, they alter heat dissipation as well as resulting temperatures. In the base case, the velocity of the background flow is $2.0 \cdot 10^{-7}$ m s^{-1} (Fig. 10), whereas near the basin, particularly at the corners, they span a range of $5.2 \cdot 10^{-9}$ m s^{-1} to $1.0 \cdot 10^{-6}$ m s^{-1}. For a given steeper hydraulic gradient (scenario G50), the range of flow

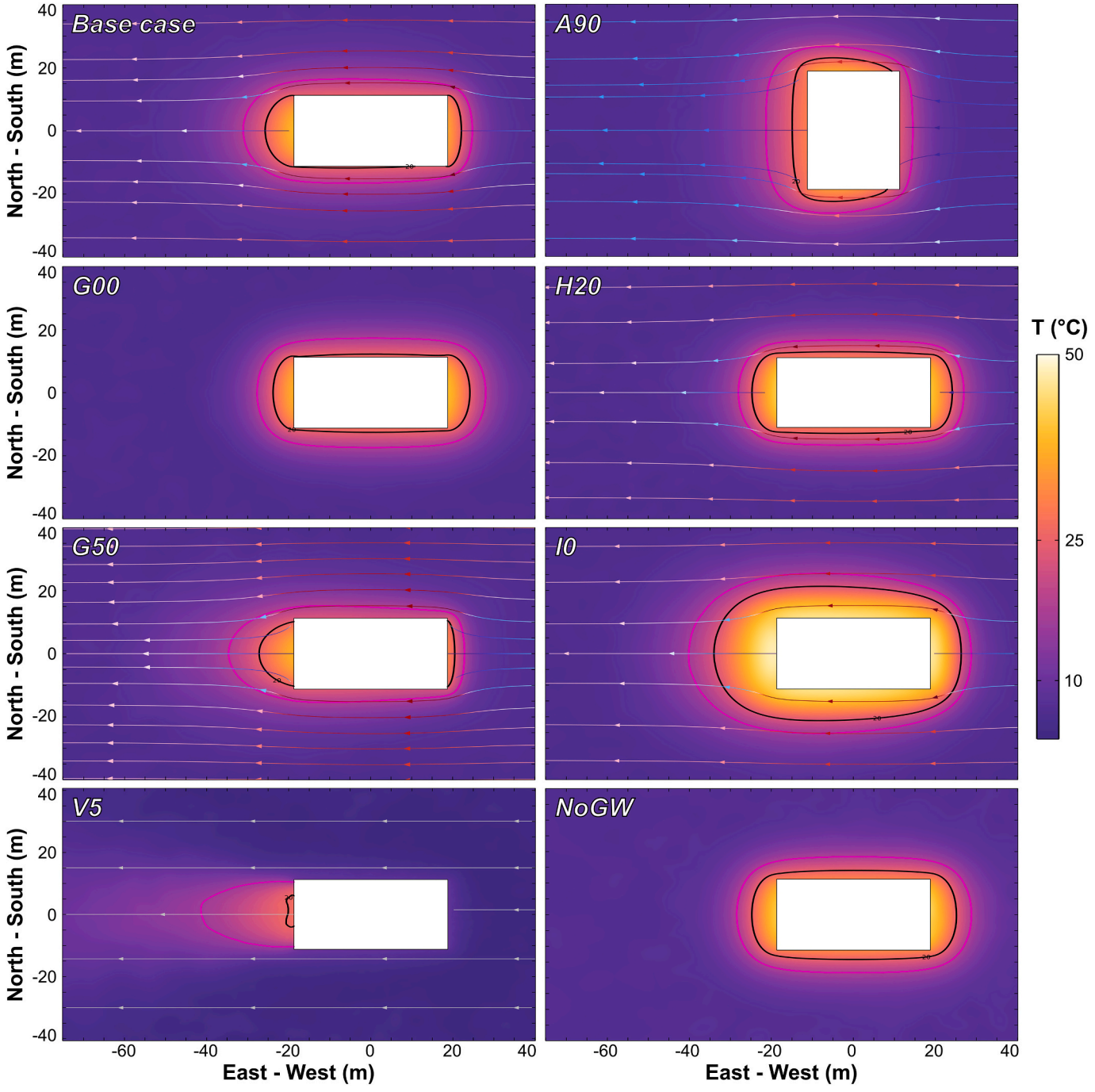

Fig. 10. Impacts of sTES on its surrounding environment: 20 °C (black) and + 6 K (magenta) thermocline around sTES at a height of $0.5 \cdot h_{sTES}$ after 10 years of operation for each scenario (cf. Table 3). (For interpretation of the references to color in this figure legend, the reader is referred to the web version of this article.)

velocities is increased to $1.3 \cdot 10^{-8}$ m s^{-1} to $2.6 \cdot 10^{-6}$ m s^{-1}, resulting in an extensive spreading of the thermal plume.

For a straightforward comparison, soil temperatures are evaluated at the same distance of 2 m (Fig. 9, top) and 5 m downstream (Fig. 9, bottom). Here, for all scenarios, the overprint due to the sTES operation becomes apparent to different extents: in the extreme case of an uninsulated sTES, temperatures of 48.1 °C are obtained. Simulations by Dahash et al. [81] yielded similar values of up to 50 °C near an uninsulated PTES at the same distance.

Among the insulated scenarios with groundwater flow, the temperatures for scenario H20 rise the highest: after 10 years of operation, the surrounding subsurface heats up to 31.3 °C. In turn, in scenario V5, with the highest heat dissipation due to groundwater flow, this increase reaches only 17.8 °C. Across all insulated scenarios, the temperature recordings show the highest amplitude (ca. 10.3 K), which is in turn only 1.4 K for scenario A90 with perpendicular groundwater flow. For the scenario without groundwater, even higher values of 31.4 °C can be observed. This is because solely conductive heat transport (i.e., absence of advection) leads to lower effective thermal conductivity, increased dissipation of thermal energy, and higher temperatures. Thus, high intensities of groundwater flows lead to lower maximum temperatures in the surrounding subsurface, but to a larger impact area. For active geothermal subsurface utilization, similar characteristics have been reported, e.g., by Hähnlein et al. [82] in the case of borehole heat exchangers, but they were so far not reported for any WGTES.

For a better-resolved evaluation, Fig. 10 shows the 20 °C and the +6 K thermocline (legally binding in Austria and recommended in Germany [45,70]) in a horizontal cut plane at half the sTES' height after 10 years. Again, the uninsulated scenario represents an extreme case, where the impact of the +6 K thermocline reaches a large maximum distance of 21.7 m. In general, downstream propagations are much greater than in the upstream direction (20 °C/6 K thermocline distance in the base case: 7.2 m/12.5 m vs. 3.3/5.9 m). Due to the perpendicular angle of inflow $\beta = 90°$ in scenario A90, a larger and broader heat plume results (downstream/lateral distances of 6 K thermocline: 10.0 m/7.5 m, vs. 5.9 m/4.9 m in the base case). In comparison, the scenario without groundwater yields extents of 2.4 m and 6.9 m (long side), and 6.1 m and 9.7 m (short side).

Generally, the shape of the resulting thermal plumes (Fig. 10) is vastly different: while the NoGW scenario leads to a very homogeneous distribution, with an increase in groundwater flow velocity, this becomes more non-uniform, but also less intense. For approval processes and further analysis, the observed temperature distributions are significant, since the measurement location has a major influence. Consequently, this issue must be highlighted as a critical lack in the heterogeneous regulatory frameworks. An accurate, 3D spatial evaluation of impacts is essential to accurately assess environmental effects. In contrast, a limitation to point measurements cannot consider heterogeneous underground conditions.

Increased temperatures can potentially affect the near field of the storage tank. Depending on the distance and respective material properties, they could exert positive effects, e.g., by preventing freezing in the vicinity and thus extending the lifetime of structures. Conversely, however, the altered conditions might pose risks, as excessive temperature fluctuations can decrease the lifetimes of subsurface-built structures.

Besides, resulting temperature conditions in the close surroundings of the storage facility potentially affect the groundwater ecosystem for all scenarios, as temperature directly impacts the physicochemical characteristics of the habitat groundwater, such as pH and oxygen concentration [55,83]. Groundwater ecosystems host a highly specialized cold-stenotherm invertebrate community and *meso*−/psychrophilic microorganisms adapted to naturally stable conditions [49,84]. A temperature change of 5–10 K is generally considered to be an acceptable range [55,85], while some studies indicate that even minor changes of 5 K may impact faunal abundance and microbial biodiversity. For example, [85] defined a thermal threshold value of 16 °C, above which no individuals of the investigated groundwater fauna species showed survival or residence in a laboratory experiment. In a field study by [86] in the Upper Rhine Plain, Germany, the diversity of crustaceans decreased significantly when groundwater temperatures exceeded a 14 °C threshold. In another field study, [48] observed decreased faunal and bacterial diversity in wells located in a thermal plume of up to 17 °C. Still, only a part of the total variability was controlled by temperature change, whereby the authors concluded that ecosystem functioning is not threatened by thermal energy discharge. Applying these findings to the thermal impacts of sTES modeled in this study, it can be summarized that ecological impacts outside of the +6 K isotherm are likely to be minor and do not deteriorate ecosystem functioning. However, the vicinity that undergoes significant thermal alteration may be affected more remarkably. The extent to which this temperature change influences physical and biotic factors of groundwater habitats still needs to be researched. Moreover, additional heat alters the chemical composition and quality of the groundwater, for example through changed mineral dissolution or contaminant transport and biodegradation [46,47,49,87].

Although the aquifer is only affected at a local scale, the storage can still contribute as a heat source to regionally elevated subsurface temperatures. Here, high subsurface temperatures above 20 °C can lead to enhanced bacterial growth, especially in drinking water distribution networks, the placement of which should be considered in the planning of sTES [51,88]. Thresholds regarding absolute temperatures or induced changes are still controversial in science [89] and inconsistent in national legislation, resulting in the absence of legally binding regulations in most countries (Fig. 2c [45]). Also, from this perspective, specific design recommendations for mitigation of environmental impacts caused by the sTES under groundwater influence can be concluded. On the one hand, high-quality, water-resistant insulation materials at all interfaces are the key measure for reducing sizes of resulting thermal plumes. On the other hand, especially for high steep hydraulic gradients, measures for controlling the local groundwater flow velocities (e.g., cut-off walls, or technical installations, such as downstream shallow geothermal installations) can be envisaged to effectively limit the impact areas of sTES.

4. Conclusions and outlook

This study provided a new (co-)simulation framework to improve the design and understanding of ambient ground thermal effects of sTES. Using a co-simulation approach between COMSOL and MATLAB/Simulink, the previously introduced STORE model for ground-based sTES was expanded to include subsurface hydrogeological processes (e.g., groundwater flow) and further environmental interactions. Thereby, the STORE model was further enhanced (e.g., inversed thermocline effect) and extended (e.g., static roof component). The merits of the newly presented framework extend beyond a refinement of the previous model version. By coupling both domains, analyses that were hitherto not possible are now available. Firstly, this concerns actual interactions of internal storage processes with the environment, that cannot be resolved with previous methods. Secondly, the framework provides fast, flexible, yet reliable guidance for planning of new installations and evaluation of existing systems.

A parameter study demonstrated the tool's versatility and applicability. Even though impacts depend on site-specific conditions, the results proved that groundwater flow can have a significant impact: Compared to a scenario without groundwater, in the worst case, the storage efficiency of an insulated sTES can decrease from 51 % to 34 %. Parameter variations (e.g., groundwater inflow angle and velocity, table depth) provided further insights into their impact, that had not been addressed so far. A change in flow velocity is most sensitive and leads to increased losses (374 MWh vs. 241 MWh in the base case). As one derived design recommendation, insulation of WGTES is indispensable

for effectively preventing thermal losses (efficiency drops to 23 % for an uninsulated sTES), and future studies are recommended to focus on the sensitivity of different insulation strategies and their impact on efficiency in different hydrogeological settings. In contrast, sTES operation can potentially cause negative implications for its surroundings, especially for groundwater ecosystems. To this end, the new framework opens unprecedented capabilities for three-dimensional spatial analysis of impacts under heterogeneous conditions and asymmetric environmental processes, which may be relevant for approval. Here, it was revealed that, despite sound insulation, a temperature increase of up to 20 °C can occur at a distance of 7.5 m after 10 years. However, this increase was limited to 18 °C under favorable conditions (i.e., vast dissipation by groundwater with high flow velocity).

In practice, heterogeneous subsurface conditions resulted in increased uncertainties in operation predictions. Thus, the evaluation of 3D propagations of thermal losses using simulation frameworks as presented was to be recommended. For further development, the remaining shortcomings of this framework (e.g., surrounding district, presence of buildings on the surrounding ground surface, and the actual topography) need to be addressed, since buildings and more complex, heterogeneous subsurface structures can have a significant influence on groundwater flow and thermal regimes. Future studies should further investigate in detail the sensitivity of initial conditions and errors of site-specific parameters (e.g., material characteristics, hydrogeological setup), based on site-specific case studies. Besides, open questions concern reconciling the accuracy of results and computational efforts by dynamic time stepping.

CRediT authorship contribution statement

Christoph Bott: Writing – review & editing, Writing – original draft, Visualization, Validation, Software, Methodology, Investigation, Funding acquisition, Formal analysis, Conceptualization. **Abdulrahman Dahash:** Writing – review & editing, Validation, Methodology, Conceptualization. **Maximilian Noethen:** Writing – review & editing, Validation, Investigation. **Peter Bayer:** Writing – review & editing, Supervision, Resources, Project administration, Funding acquisition, Conceptualization.

Declaration of competing interest

The authors declare that they have no competing financial interests or personal relationships that could have appeared to influence the work reported in this paper.

Data availability

All relevant data is attached. Other data can be made available on request.

Acknowledgments

The authors acknowledge Ryan Pearson for language edits. The present study is financially supported by the EU Horizon Europe project INTERSTORES (project no. 101136100).

Appendix A. Model validation

The applicability of the STORE model to capture the operational behavior of WGTES was tested in the preceding study by Bott et al. [54]. Further, in an additional validation process described below, the co-simulation approach was compared with a proven approach. With this, the applicability of the newly developed framework to the later deployments for parameter and sensitivity studies was proven.

Model description

For the validation, a traditional COMSOL model is used in which the effects of seasonal storage are implemented as temperature boundary conditions. The geometry of the basin is maintained and the height-resolved temperature differences (due to the temperature stratification present in the filling) are also accounted for. The STORE model previously tested in Bott et al. [64] is used to generate a temperature profile corresponding to each layer of the external wall of the storage tank, as well as for the top and the bottom surfaces. These temperature profiles are used as transient boundary conditions, as commonly used in state-of-the-art sTES models. Subsequently, the storage operation is simulated on the one hand using the co-simulation approach and on the other hand using the temperature data in a test case described below. In this context, it should be noted that the compared variant cannot represent feedback reactions to the storage facility and that the long-term changed conditions (e.g., less energy required to operate the storage because the surrounding ground is heated up) are deviating. As a result, the thermal mass of the storage facility itself, which is influenced by the changing temperature field of the surrounding subsurface during charging and discharging processes, is not considered in the traditional method.

Test case

Despite the above-described differences, to test the new model, a generic test case is generated. From this, general conclusions about the general effects of the newly implemented mechanisms of the model become apparent. The geometry of the storage covers dimensions of 80 × 80 × 15 m and a slope angle of 45°, resulting in a volume of ca. 45,000 m^3. Material parameters are not varied and are generally representative values for average conditions in the subsoil of construction sites.

The storage facility for the validation scenario is assumed to be a low-insulated water-gravel thermal energy storage facility (0.1 m foam glass gravel on all sides), with the static component measuring additionally 0.25 m of concrete on all sides. The storage facility is designed to have a top cover with a thickness of 1 m and a slope angle of 1:2. For the operation of the unit, pipe coil systems made from PE-X on 3 levels with a spacing of 1 m and a hydraulic diameter of 0.05 m are considered. The resulting surface area of the heat exchanger is thus 18,798 m^2 with a length of ca. 5906 m.

The hourly resolved load profiles shown in Fig. A-1 are used for the operation simulation, which starts on April 1 (end of the heating period) with a charging of the storage.

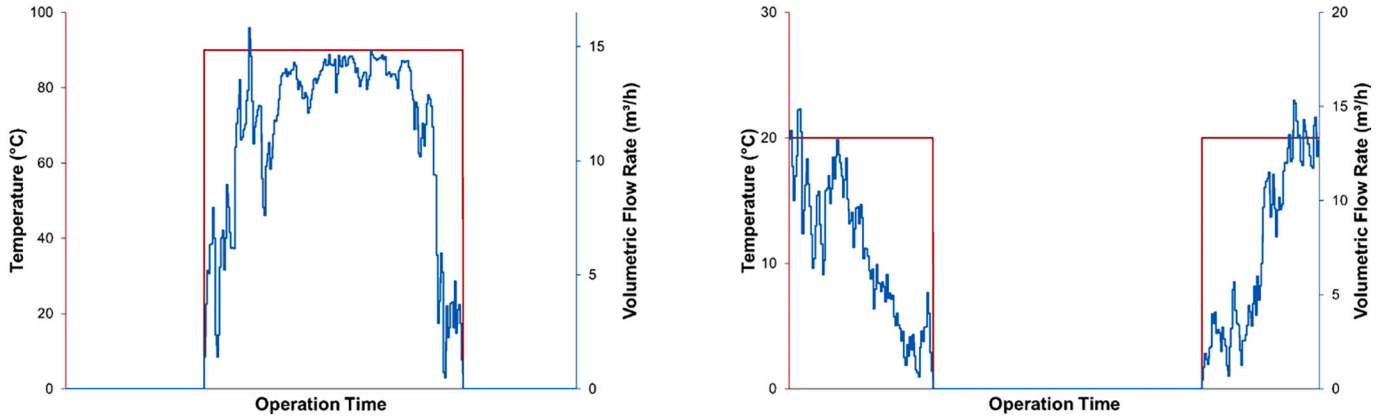

Fig. A-1. Charging (left) and discharging (right) operational load profiles used in the validation.

The environmental temperature profile is shown in Fig. A-2 and consist of a sinusoidal function according to the equation $T_{air}(h)[^{\circ}C] = 10 - 10 \cdot cos\frac{2 \cdot \pi \cdot t\,[h]}{8760\,[h]}$. To represent seasonally and daily varying solar irradiation, the following equation is used:

$$\ddot{q}_{sol}(h)\left[\frac{W}{m^2}\right] = 0.8 - 0.8 \cdot \frac{2 \cdot \pi \cdot t\,[h]}{24\,[h]} + 0.8 - 0.8 \cdot \frac{2 \cdot \pi \cdot t\,[h]}{8760\,[h]}$$

Besides, the environmental boundary conditions of precipitation and convective heat loss based on wind velocities are disabled.

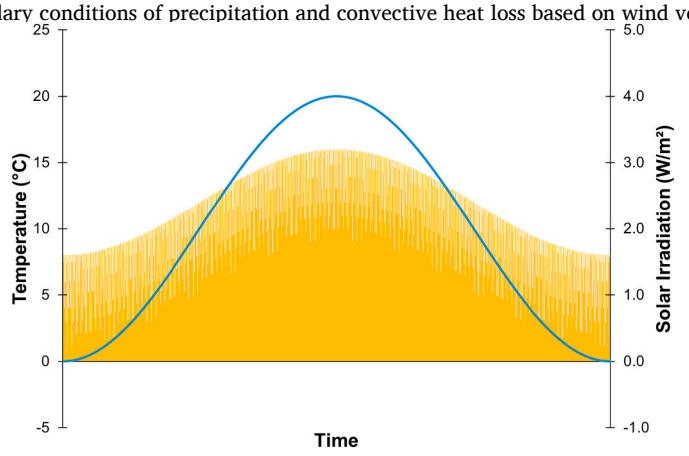

Fig. A-2. Environmental boundary condition datasets (ambient temperature: blue, solar irradiation: yellow) used in the validation.

As in the STORE model, a homogeneous subsurface of dry soil is assumed in the COMSOL model for the co-simulation. Appropriately, no groundwater flow conditions are assumed in the validation. The simulation period covered is 5 years, with time steps of 24 h being used in COMSOL. The distances to the model boundaries in COMSOL are 200 m to all sides and 30 m to the ground, the resulting mesh (automatically generated with settings default "fine") consists of 31,355 elements (average skewness quality: 0.55).

Validation results

For the evaluation of the results, and comparison of the two methods, focus is first placed on the differences in the thermal losses (Fig. A-3). Over the entire simulation period of 5 years, the differences in heat losses are on average − 0.83 kW, whereby positive and negative deviations offset each other. The validation (traditional model) generally leads to lower heat losses, with a maximum of 183.28 kW higher heat losses in the co-simulation, yielding a more pessimistic outcome. The range of values in the co-simulation is 238.04 kW (−177.50 kW to +60.54 kW) and in the validation 213.75 kW (−178.68 kW to +35.06 kW). In total, the largest deviations (up to 395.68 kW) occur at the top of the storage facility. This is plausible since the highest storage temperatures and largest temperature differences to the environment occur here. Consequently, the effects on the newly implemented mechanisms in the subsurface, especially the interaction with hydrogeological boundary conditions, are less influenced at the same time.

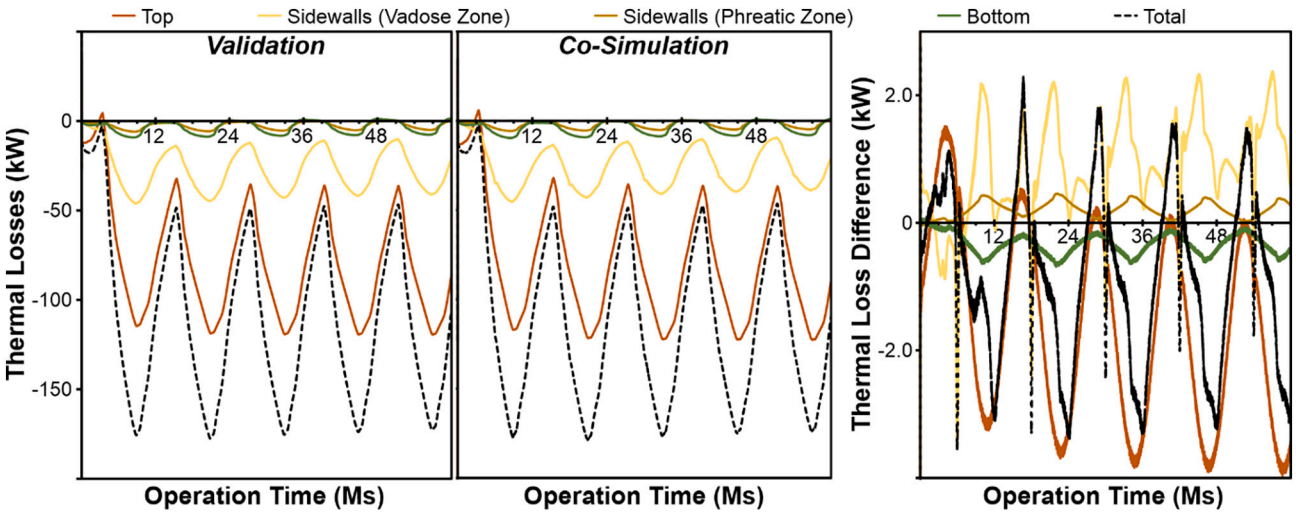

Fig. A-3. Results of observed thermal energy losses in the validation. Left, center: Thermal losses for the top, sidewalls, and bottom section of the simulated storage operation. Right: Heat loss difference between the co-simulation and the validation. Ms: months.

Similarly, the resulting temperatures in the subsurface show a quite similar pattern for both variants (Fig. A-4). At a distance of 5 m next to the side wall, temperature characteristics are compared at different depths (2 m to 10 m as well as 25 % to 75 % of the sTES height), as well as 1 m below the center of the foundation. Thereby it can be seen that the deviations for all values next to the storage facility are below 1 K (−0.95 K to +0.93 K). On average, they only differ by 0.30 K. In contrast, the results below the storage foundation show up to three times higher deviations (−0.05 K to 3.12 K).

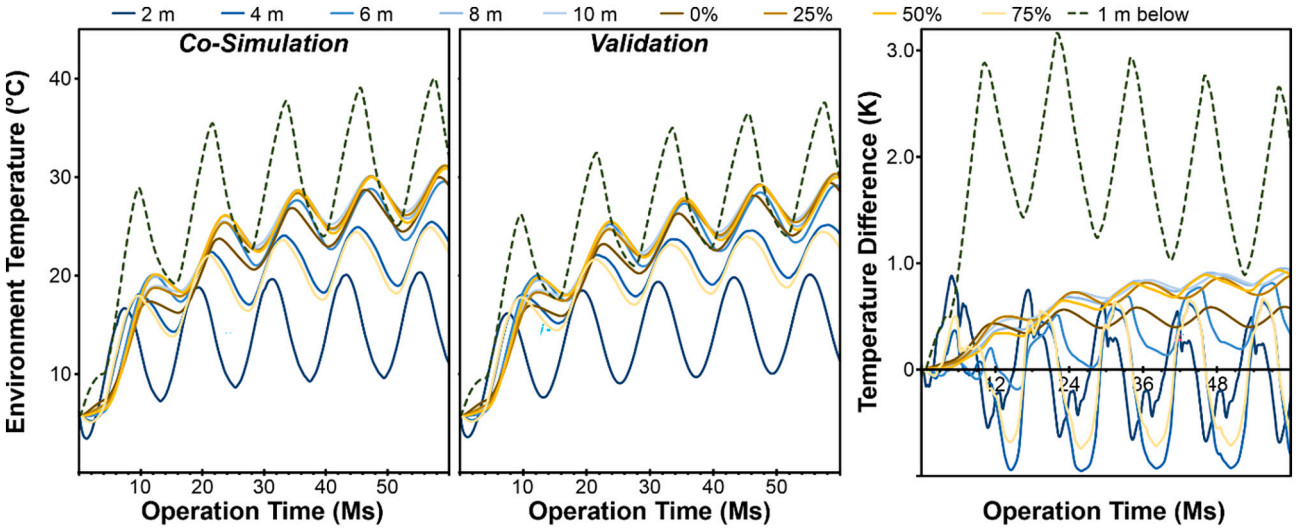

Fig. A-4. Results of observed temperatures in the validation. Left, center: 5 m next to the seasonal thermal energy storage's sidewalls in different depths, as well as 1 m below the storage's foundation. Right: Temperature difference of the co-simulation and the validation. Ms: months.

However, this is because the coupling of a transient temperature boundary condition at the bottom surface of the storage facility has a different effect than heat loss which better reflects the interference at the boundary (transition to the side walls). This is also clearly visible in the sectional view of Fig. A-5.

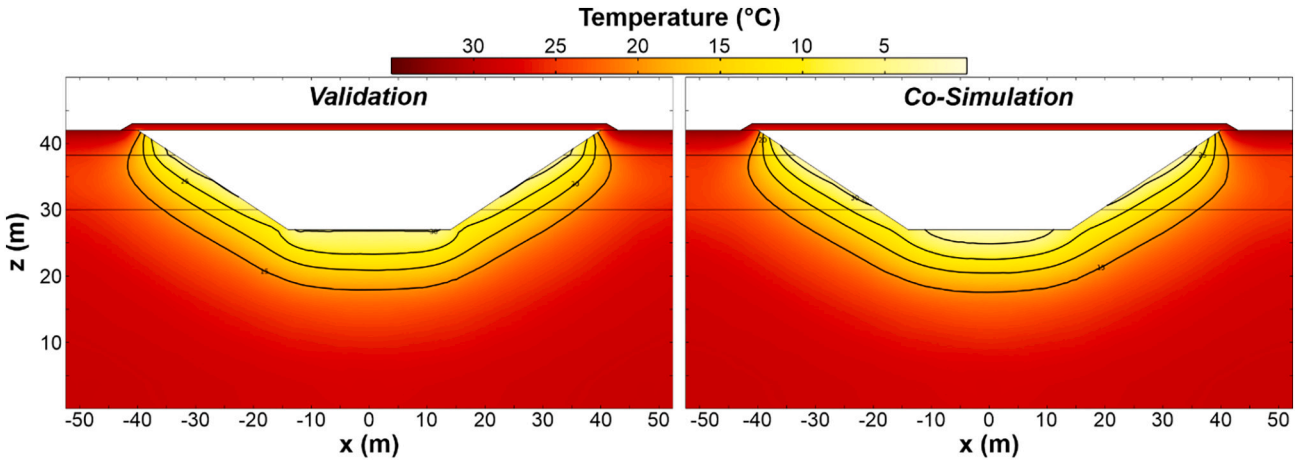

Fig. A-5. Results of observed underground temperatures in a cross-sectional view for the validation (left) and the co-simulation (right).

By comparing the newly developed tool, which is based on the approach already tested by Bott et al. [64], with a well-proven alternative for modeling temperature impacts, it can be summarized that divergences are low. Thus, the applicability of the advanced modeling method is demonstrated, while remaining uncertainties can be attributed to the weaknesses of the validation variant. The latter is not able to represent the interactions of a storage facility and environment as well as spatially resolved interferences of the heat losses themselves very well.

Appendix B. Mesh refinement

To enable a sufficiently accurate simulation of the hydrogeological situation under the highly dynamic conditions of a seasonal thermal energy storage (sTES) operation, the mesh needs to be subject to refinements. Therefore, during the development of the newly presented framework, a dedicated investigation of the mesh quality of the numerical 3D-multiphysics model for the environmental domain was performed. In this process, several meshes and refinements were iteratively tested, compared, and evaluated, according to established quality criteria (e.g., skewness, radii, volume vs. circumference). Results showed that, particularly in the near field of the storage, strong temperature gradients are to be expected, so a higher resolution is necessary there. Based on this investigation, a temperature gradient-based mesh refinement method was deduced and is to be recommended, together with further modifications, as explained in the following sections. This ensures an improved quality of the results while at the same time being adaptable to various (e.g., geometric) setups when the framework is applied to specific site conditions.

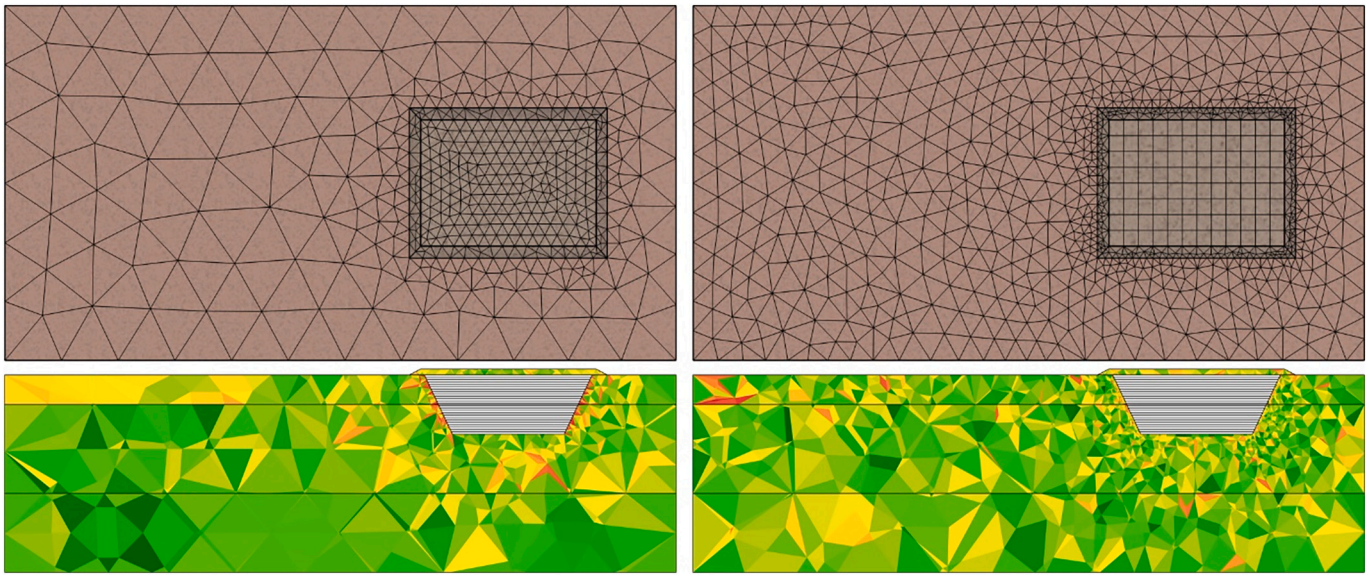

Fig. B-1. COMSOL mesh before (left) and after (right) gradient-based refinement in top (upper) and cross-sectional view (lower, color bar indicating skewness quality of elements, from red (low quality) to green (high quality)).

First, four boundary layers with a thickness increase factor of 1.5 are inserted around the storage facility starting from an initial layer thickness of 0.05 m, so that a good transition is achieved at the interface and in the corner area. Based on the physics-based meshing of the model geometry, it is also worth noting that the situation of groundwater flow around the sTES structure results in an asymmetric energy flux and temperature gradient distribution. Therefore, to achieve further refinement of the mesh in the thermal plume generated by groundwater flow, a temperature gradient-based refinement is introduced. For this purpose, a steady-state study is performed in advance. A constant environmental temperature (initial conditions), the average expected heat losses of the basin, and the maximum gradients of the hydraulic heads are assumed. After the simulation of this test, resulting temperature gradients in the model's domains are reported and subsequently used for an error-based refinement. Preliminary investigations

revealed that a refinement above a limit of $\Delta T > 2$ K significantly improves the later, real transient simulation results. Consequently, this refined mesh is designed for extreme situations and adapted to the specific site considered. Nevertheless, it has to be considered that even this method involves a degree of uncertainty in the model setup, which might need to be checked within a further sensitivity analysis when applying the framework to other site-specific conditions.

Appendix C. Supplementary data

Supplementary data to this article can be found online at https://doi.org/10.1016/j.est.2024.112222.

References

[1] A. Dahash, F. Ochs, M.B. Janetti, W. Streicher, Advances in seasonal thermal energy storage for solar district heating applications: a critical review on large-scale hot-water tank and pit thermal energy storage systems, Appl. Energy 239 (2019) 296–315, https://doi.org/10.1016/j.apenergy.2019.01.189.

[2] I. Sifnaios, D.M. Sneum, A.R. Jensen, J. Fan, R. Bramstoft, The impact of large-scale thermal energy storage in the energy system, Appl. Energy 349 (2023) 121663, https://doi.org/10.1016/j.apenergy.2023.121663.

[3] M. Sun, T. Liu, X. Wang, T. Liu, M. Li, G. Chen, D. Jiang, Roles of thermal energy storage technology for carbon neutrality, Carbon Neutrality 2 (2023), https://doi.org/10.1007/s43979-023-00052-w.

[4] S. Zhang, P. Ocłoń, J.J. Klemeš, P. Michorczyk, K. Pielichowska, K. Pielichowski, Renewable energy systems for building heating, cooling and electricity production with thermal energy storage, Renew. Sust. Energ. Rev. 165 (2022) 112560, https://doi.org/10.1016/j.rser.2022.112560.

[5] C. Bott, I. Dressel, P. Bayer, State-of-technology review of water-based closed seasonal thermal energy storage systems, Renew. Sust. Energ. Rev. 113 (2019) 109241, https://doi.org/10.1016/j.rser.2019.06.048.

[6] D. Mangold, L. Deschaintre, Seasonal Thermal Energy Storage: Report on State of the Art and Necessary Further R+D, 2015.

[7] International Renewable Energy Agency, IRENA-IEA-ETSAP Technology Brief 4: Thermal Storage.

[8] R. Jacob, M. Hoffmann, J.M. Weinand, J. Linßen, D. Stolten, M. Müller, The future role of thermal energy storage in 100% renewable electricity systems, Renewable and Sustainable Energy Transition 4 (2023) 100059, https://doi.org/10.1016/j.rset.2023.100059.

[9] R. Kübler, N. Fisch, E. Hahne, High temperature water pit storage projects for the seasonal storage of solar energy, Sol. Energy 61 (1997) 97–105.

[10] L. Xu, J.I. Torrens, F. Guo, X. Yang, J.L. Hensen, Application of large underground seasonal thermal energy storage in district heating system: a model-based energy performance assessment of a pilot system in Chifeng, China, Appl. Therm. Eng. 137 (2018) 319–328, https://doi.org/10.1016/j.applthermaleng.2018.03.047.

[11] S. Boesten, W. Ivens, S.C. Dekker, H. Eijdems, 5th generation district heating and cooling systems as a solution for renewable urban thermal energy supply, Adv. Geosci. 49 (2019) 129–136, https://doi.org/10.5194/adgeo-49-129-2019.

[12] S. Chavan, V. Panwar, R. Rathod, Review on thermal energy storage techniques, International Journal of Engineering Development and Research 3 (2015) 944–948.

[13] A. Hesaraki, S. Holmberg, F. Haghighat, Seasonal thermal energy storage with heat pumps and low temperatures in building projects—a comparative review, Renew. Sust. Energ. Rev. 43 (2015) 1199–1213, https://doi.org/10.1016/j.rser.2014.12.002.

[14] S. Koohi-Fayegh, M.A. Rosen, A review of energy storage types, applications and recent developments, Journal of Energy Storage 27 (2020) 101047, https://doi.org/10.1016/j.est.2019.101047.

[15] S. Bespalko, A. Munoz Minarnda, O. Halychyi, Overview of the existing heat storage technologies: sensible heat 28 (2018) 82–113.

[16] R. Radloff, Weltgrößte Solarthermieanlage in Vojens, Wärmewände-Info, 2015, pp. 1–4.

[17] J. Ríos-Arriola, N. Velázquez-Limón, J.A. Aguilar-Jiménez, S. Islas, J.D. López-Sánchez, F.J. Caballero-Talamantes, J.A. Corona-Sánchez, C.A. La Cásares-De Torre, Comparison between air-exposed and underground thermal energy storage for solar cooling applications, Processes 11 (2023) 2406, https://doi.org/10.3390/pr11082406.

[18] A.V. Novo, J.R. Bayon, D. Castro-Fresno, J. Rodriguez-Hernandez, Review of seasonal heat storage in large basins: water tanks and gravel–water pits, Appl. Energy 87 (2010) 390–397, https://doi.org/10.1016/j.apenergy.2009.06.033.

[19] F. Ochs, W. Heidemann, H. Müller-Steinhagen, H. Koch, Erdreich/Wasser-Edbecken-Wärmespeicher mit direktem Beladesystem, in: OTTI, 16. Symposium thermische Solarenergie, Kloster Banz, Bad Staffelstein, Germany, 2006.

[20] M. Benner, M. Bodmann, D. Mangold, J. Nußbicker, S. Raab, T. Schmidt, H. Seiwald, Solar unterstützte Nahwärmeversorgung mit und ohne Langzeit-Wärmespeicher: Forschungsbericht zum BMBF/BMWA-Vorhaben; (November 1998 bis Januar 2003), Stuttgart, 2003.

[21] M.V. Jensen, J.E. Nielsen, Seasonal pit heat storages - guidelines for materials & construction: IEA SHC Fact Sheet 55.C-D2, 2020.

[22] F. Ochs, A. Dahash, A. Tosatto, M. Bianchi Janetti, Techno-economic planning and construction of cost-effective large-scale hot water thermal energy storage for Renewable District heating systems, Renew. Energy 150 (2020) 1165–1177, https://doi.org/10.1016/j.renene.2019.11.017.

[23] G.K. Dolgun, A. Keçebaş, M. Ertürk, A. Daşdemir, Optimal insulation of underground spherical tanks for seasonal thermal energy storage applications, Journal of Energy Storage 69 (2023) 107865, https://doi.org/10.1016/j.est.2023.107865.

[24] A. Heller, Floating Lid Constructions for Pit Water Storage - A Survey, Report R-011, Technical University of Denmark, Department of Civil Engineering, Copenhagen, Denmark, 1997.

[25] A. Tosatto, F. Ochs, A. Dahash, C. Muser, F. Kutscha-Lissberg, P. Kremnitzer, Influence of heat and mass transfer on the performance of large-scale thermal energy storage systems, in: P. Schossig, P. Droege, A. Riemer, M. Speer (Eds.), Proceedings of the International Renewable Energy Storage Conference (IRES 2022), Atlantis Press International BV, Dordrecht, 2023, pp. 470–488.

[26] I. Sifnaios, A.R. Jensen, S. Furbo, J. Fan, Heat losses in water pit thermal energy storage systems in the presence of groundwater, Appl. Therm. Eng. 235 (2023) 121382, https://doi.org/10.1016/j.applthermaleng.2023.121382.

[27] O. Abdelhak, H. Mhiri, P. Bournot, CFD analysis of thermal stratification in domestic hot water storage tank during dynamic mode, Build. Simul. 8 (2015) 421–429, https://doi.org/10.1007/s12273-015-0216-9.

[28] S. Göppert, R. Lohse, T. Urbaneck, U. Schirmer, B. Platzer, Forschungsbericht - Solarthermie 2000plus - Weiterentwicklung und Optimierung von Be- und Entladesystemen für Tank- und Erdbeckenspeicher: 2004–2008, Techn. Univ, Chemnitz, Ilmenau, 2009.

[29] C. Zhu, J. Zhang, Y. Wang, Z. Deng, P. Shi, J. Wu, Z. Wu, Study on thermal performance of single-tank thermal energy storage system with thermocline in solar thermal utilization, Appl. Sci. 12 (2022) 3908, https://doi.org/10.3390/app12083908.

[30] J. Allegrini, K. Orehounig, G. Mavromatidis, F. Ruesch, V. Dorer, R. Evins, A review of modelling approaches and tools for the simulation of district-scale energy systems, Renew. Sust. Energ. Rev. 52 (2015) 1391–1404, https://doi.org/10.1016/j.rser.2015.07.123.

[31] D. Olsthoorn, F. Haghighat, P.A. Mirzaei, Integration of storage and renewable energy into district heating systems: a review of modelling and optimization, Sol. Energy 136 (2016) 49–64, https://doi.org/10.1016/j.solener.2016.06.054.

[32] Y. Zhang, Applicability of Thermal Energy Storage in Future District Heating System - Design Methodologies and Performance Evaluations, 2021 (Thesis for the degree of licentiate of engineering, Gothenburg, Sweden).

[33] A.G. Olabi, A.A. Abdelghafar, H.M. Maghrabie, E.T. Sayed, H. Rezk, M.A. Radi, K. Obaideen, M.A. Abdelkareem, Application of artificial intelligence for prediction, optimization, and control of thermal energy storage systems, Thermal Science and Engineering Progress 39 (2023) 101730, https://doi.org/10.1016/j.tsep.2023.101730.

[34] G. de Goeijen, Developing a Method for the Operational Control of an Ecovat System, 2019.

[35] A. Tosatto, A. Dahash, F. Ochs, Simulation-based performance evaluation of large-scale thermal energy storage coupled with heat pump in district heating systems, Journal of Energy Storage 61 (2023) 106721, https://doi.org/10.1016/j.est.2023.106721.

[36] R. Marx, J. Nußbicker-Lux, D. Bauer, W. Heidemann, H. Drück, Saisonale Wärmespeicher - Bauarten, Betriebsweise und Anwendungen, Chem. Ing. Tech. 83 (2011) 1994–2001, https://doi.org/10.1002/cite.201100064.

[37] J. Nußbicker-Lux, R. Marx, D. Bauer, H. Drück, Lektionen aus Planung und Betrieb von drei Deutschen solaren Nahwärmeversorgungen mit saisonaler Wärmespeicherung, in: Gleisdorf Solar 2012, 10. Internationale Konferenz für thermische Solarenergienutzung, Gleisdorf, 12.-14.09.2012, 2012.

[38] M. Schlosser, M. Heuer, M.N. Fisch, Langzeitmonitoring Solar unterstützte Nahwärmeversorgung Hamburg-Bramfeld, in: E.ON Hanse Wärme, 25.07.2007, 2007.

[39] E. Hahne, The ITW solar heating system: an oldtimer fully in action, Sol. Energy 69 (2000) 469–493, https://doi.org/10.1016/S0038-092X(00)00115-8.

[40] L. Hermans, R. Haesen, A. Uytterhoeven, W. Peere, W. Boydens, L. Helsen, Pre-design of collective residential solar districts with seasonal thermal energy storage: importance of level of detail, Appl. Therm. Eng. 226 (2023) 120203, https://doi.org/10.1016/j.applthermaleng.2023.120203.

[41] F. Ochs, A. Dahash, A. Tosatto, M. Reisenbichler, K. O'Donovan, G. Gauthier, C. K. Skov, T. Schmidt, Comprehensive comparison of different models for large-scale thermal energy storage, in: Proceedings of the International Renewable Energy Storage Conference 2021 (IRES 2021), Global Online Event, Germany, Atlantis Press, Paris, France, 2022, pp. 36–51.

[42] A. Dahash, F. Ochs, A. Tosatto, W. Streicher, Toward efficient numerical modeling and analysis of large-scale thermal energy storage for renewable district heating, Appl. Energy 279 (2020) 115840, https://doi.org/10.1016/j.apenergy.2020.115840.

[43] C. Bott, I. Dressel, P. Bayer, In-ground Closed, Water-based seasonal storage systems for thermal energy - "state-of-technology in Europe", in: Proceedings World Geothermal Congress 2020, Reykjavik, Iceland, The Hague, The Netherlands, 2020.
[44] M. Bodmann, M.N. Fisch, Solar unterstützte Nahwärmeversorgung: Pilotprojekte Hamburg, Hannover und Steinfurt, in: 5. FKS-Symposium: FKS-Forschungskreis Solarenergie TU Braunschweig, Braunschweig, 17.-18.06.2004, 2004.
[45] S. Haehnlein, P. Bayer, P. Blum, International legal status of the use of shallow geothermal energy, Renew. Sust. Energ. Rev. 14 (2010) 2611–2625, https://doi.org/10.1016/j.rser.2010.07.069.
[46] M. Bonte, P.J. Stuyfzand, G.A. van den Berg, W.A.M. Hijnen, Effects of aquifer thermal energy storage on groundwater quality and the consequences for drinking water production: a case study from The Netherlands, Water Sci. Technol. 63 (2011) 1922–1931, https://doi.org/10.2166/wst.2011.189.
[47] C. Beyer, S. Popp, S. Bauer, Simulation of temperature effects on groundwater flow, contaminant dissolution, transport and biodegradation due to shallow geothermal use, Environ. Earth Sci. 75 (2016), https://doi.org/10.1007/s12665-016-5976-8.
[48] H. Brielmann, C. Griebler, S.I. Schmidt, R. Michel, T. Lueders, Effects of thermal energy discharge on shallow groundwater ecosystems, FEMS Microbiol. Ecol. 68 (2009) 273–286, https://doi.org/10.1111/j.1574-6941.2009.00674.x.
[49] J. Becher, C. Englisch, C. Griebler, P. Bayer, Groundwater fauna downtown - drivers, impacts and implications for subsurface ecosystems in urban areas, J. Contam. Hydrol. 248 (2022) 104021, https://doi.org/10.1016/j.jconhyd.2022.104021.
[50] T. Lienen, K. Lüders, H. Halm, A. Westphal, R. Köber, H. Würdemann, Effects of thermal energy storage on shallow aerobic aquifer systems: temporary increase in abundance and activity of sulfate-reducing and sulfur-oxidizing bacteria, Environ. Earth Sci. 76 (2017), https://doi.org/10.1007/s12665-017-6575-z.
[51] C.M. Agudelo-Vera, M. Blokker, H. de Kater, R. Lafort, Identifying (subsurface) anthropogenic heat sources that influence temperature in the drinking water distribution system, Drink. Water Eng. Sci. 10 (2017) 83–91, https://doi.org/10.5194/dwes-10-83-2017.
[52] M. Noethen, H. Hemmerle, P. Bayer, Sources, intensities, and implications of subsurface warming in times of climate change, Crit. Rev. Environ. Sci. Technol. 53 (2023) 700–722, https://doi.org/10.1080/10643389.2022.2083899.
[53] A. Dahash, F. Ochs, G. Giuliani, A. Tosatto, Understanding the interaction between groundwater and large-scale underground hot-water tanks and pits, Sustain. Cities Soc. 71 (2021) 102928, https://doi.org/10.1016/j.scs.2021.102928.
[54] G.J. van den Brink, C.J. Hoogendorn, Ground water flow heat losses for seasonal heat storage in the soil, Sol. Energy 30 (1983) 367–371.
[55] C. Griebler, H. Brielmann, C.M. Haberer, S. Kaschuba, C. Kellermann, C. Stumpp, F. Hegler, D. Kuntz, S. Walker-Hertkorn, T. Lueders, Potential impacts of geothermal energy use and storage of heat on groundwater quality, biodiversity, and ecosystem processes, Environ. Earth Sci. 75 (2016), https://doi.org/10.1007/s12665-016-6207-z.
[56] Alejandro García Gil, Miguel Mejías Moreno, Current legal framework on shallow geothermal energy use in Spain, J Sustain Res 2 (2019), https://doi.org/10.20900/jsr20200005.
[57] F. Stauffer, P. Bayer, P. Blum, N.M. Giraldo, W. Kinzelbach, Thermal Use of Shallow Groundwater, Online-Ausg, CRC Press, Boca Raton, Florida, 2014.
[58] A. Dahash, F. Ochs, A. Tosatto, Co-simulation of dynamic energy system simulation and COMSOL multiphysics, in: COMSOL Conference 2019, Cambridge, 2019.
[59] The Mathworks Inc, MATLAB, The Mathworks Inc., Natick, Massachusetts, USA, 2023.
[60] MathWorks, Simscape - Model and simulate multidomain physical systems (Version 5.0), 2021. https://www.mathworks.com/help/physmod/simscape/ (accessed 7 September 2021).
[61] COMSOL AB, COMSOL Multiphysics, COMSOL AB, Stockholm Sweden, 2023.
[62] The Modelica Association, Functional Mock-up Interface: The Leading Standard to Exchange Dynamic Simulation Models, The Modelica Association, Linköping, Sweden, 2023.
[63] COMSOL AB, LiveLink for Simulink: User's Guide. Version 6.1, 2021 (Stockholm Sweden).
[64] C. Bott, M. Ehrenwirth, C. Trinkl, P. Bayer, Component-based modeling of ground-coupled seasonal thermal energy storages, Appl. Therm. Eng. (2022) 118810, https://doi.org/10.1016/j.applthermaleng.2022.118810.
[65] C. Forkel, H. Daniels, Finite element simulation of circulation in large scale thermal energy storage basins, Adv. Water Resour. 18 (1995) 147–158, https://doi.org/10.1016/0309-1708(95)00007-6.
[66] H. Drück, MULTIPORT Store-Model for TRNSYS: Stratified Fluid Storage Tank With Four Internal Heat Exchangers, Ten Connections for Direct Charge and Discharge and an Internal Electrical Heater. Version 1.99F, Stuttgart, Germany, 2006.
[67] L. Mazzarella, Multi-flow Stratified Thermal Storage Model With Full-mixed Layers: Type 142, Institut für Thermodynamik und Wärmetechnik Universität Stuttgart-FRG, Stuttgart, 1992.
[68] Solar-Institut Juelich, CARNOT Toolbox: Release 8.0.1 (Matlab 2021b), Solar-Institut Juelich, FH Aachen, Aachen, 2023.
[69] A. Dahash, F. Ochs, A. Tosatto, Techno-economic and exergy analysis of tank and pit thermal energy storage for renewables district heating systems, Renew. Energy 180 (2021) 1358–1379, https://doi.org/10.1016/j.renene.2021.08.106.
[70] Verein Deutscher Ingenieure, Thermal Use of the Underground: Fundamentals, Approvals, Environmental Aspects, Beuth Verlag GmbH, Berlin, 2010.
[71] J.D. Hunt, B. Zakeri, W. Leal Filho, P.S. Schneider, N.d.A.B. Weber, L.W. Vieira, C. Ermel, N.J. de Castro, P.S.F. Barbosa, A. Nascimento, A. Mastrucci, Swimming pool thermal energy storage, an alternative for distributed cooling energy storage, Energy Convers. Manag. 230 (2021) 113796, https://doi.org/10.1016/j.enconman.2020.113796.
[72] R. Ilgaz, R. Yumrutaş, Heating performance of swimming pool incorporated solar assisted heat pump and underground thermal energy storage tank: a case study, Int. J. Energy Res. 46 (2022) 1008–1031, https://doi.org/10.1002/er.7221.
[73] I. Dressel, C. Bott, P. Bayer, Converting idle infrastructure to large scale seasonal heat storage systems, in: 45th IAH Congress, Daejeon, Korea, 2018.
[74] Ecoglas, Technische Daten. https://www.ecoglas.de/files/Technische-Daten.pdf, 2021. (Accessed 10 June 2021).
[75] C. Bott, I. Dressel, P. Bayer, Paraffin wax as self-sealing insulation material of seasonal sensible heat storage systems-a laboratory study, PLoS One 15 (2020) e0236056, https://doi.org/10.1371/journal.pone.0236056.
[76] F. Ochs, H. Müller-Steinhagen, Abschlussbericht zum Vorhaben Weiterentwicklung der Erdbecken-Wärmespeichertechnologie. FKZ 0329607 E, 2008 (Stuttgart).
[77] E. Valor, V. Caselles, Mapping land surface emissivitiy from NDVI: application to European, African, and South American areas, Remote Sens. Environ. 57 (1996) 167–184.
[78] S. Krähenmann, Handbuch: Ortsgenaue Testreferenzjahre von Deutschland für mittlere, extreme und zukünftige Witterungsverhältnisse, 2017 (Offenbach).
[79] BBSR, Ortsgenaue Testreferenzjahre (TRY) von Deutschland für mittlere und extreme Witterungsverhältnisse: Release date: 2021-06-08. Test datasets for environmental conditions, Deutscher Wetterdienst (German Weather Service), 2017 (Bonn).
[80] A. Dahash, M. Michele Bianchi Janetti, F. Ochs, Numerical analysis and evaluation of large-scale hot water tanks and pits in district heating systems, in: Proceedings of Building Simulation 2019: 16th Conference of IBPSA, IBPSA, Rome, Italy, 2020, pp. 1692–1699.
[81] A. Dahash, M. Bianchi Janetti, F. Ochs, Detailed 3-D models of a large-scale underground thermal energy storage with consideration of groundwater conditions, in: ISEC, 2018, pp. 597–604.
[82] S. Hähnlein, N. Molina-Giraldo, P. Blum, P. Bayer, P. Grathwohl, Ausbreitung von Kältefahnen im Grundwasser bei Erdwärmesonden, Grundwasser 15 (2010) 123–133, https://doi.org/10.1007/s00767-009-0125-x.
[83] T. Riedel, Temperature-associated changes in groundwater quality, J. Hydrol. 572 (2019) 206–212, https://doi.org/10.1016/j.jhydrol.2019.02.059.
[84] A. Retter, C. Karwautz, C. Griebler, Groundwater microbial communities in times of climate change, Curr. Issues Mol. Biol. 41 (2021) 509–538, https://doi.org/10.21775/cimb.041.509.
[85] H. Brielmann, T. Lueders, K. Schreglmann, F. Ferraro, M. Avramov, V. Hammerl, P. Blum, P. Bayer, C. Griebler, Oberflächennahe Geothermie und ihre potenziellen Auswirkungen auf Grundwasserökosysteme, Grundwasser 16 (2011) 77–91, https://doi.org/10.1007/s00767-011-0166-9.
[86] C. Spengler, Die Auswirkungen von anthropogenen Temperaturerhöhungen auf die Crustaceagemeinschaften im Grundwasser: Versuch einer Prognose zur Klimaerwärmung und lokalen Wärmeeinträgen, Koblenz-Landau, 2017 (PhD Thesis).
[87] A. García-Gil, E. Garrido Schneider, M. Mejías, D. Barceló, E. Vázquez-Suñé, S. Díaz-Cruz, Occurrence of pharmaceuticals and personal care products in the urban aquifer of Zaragoza (Spain) and its relationship with intensive shallow geothermal energy exploitation, J. Hydrol. 566 (2018) 629–642, https://doi.org/10.1016/j.jhydrol.2018.09.066.
[88] L. van den Bos, Quantifying the Effects of Anthropogenic Heat Sources on the Water Temperature in the Drinking Water Distribution System, 2020 (Master's Thesis, Delft, The Netherlands).
[89] P. Blum, K. Menberg, F. Koch, S.A. Benz, C. Tissen, H. Hemmerle, P. Bayer, Is thermal use of groundwater a pollution? J. Contam. Hydrol. 239 (2021) 103791 https://doi.org/10.1016/j.jconhyd.2021.103791.